

5-2020

Shape Optimization of Microfiber Composite Energy Harvesters

Suyash Lahoti

Follow this and additional works at: <https://commons.erau.edu/edt>



Part of the [Aerospace Engineering Commons](#)

Scholarly Commons Citation

Lahoti, Suyash, "Shape Optimization of Microfiber Composite Energy Harvesters" (2020). *Dissertations and Theses*. 528.

<https://commons.erau.edu/edt/528>

This Thesis - Open Access is brought to you for free and open access by Scholarly Commons. It has been accepted for inclusion in Dissertations and Theses by an authorized administrator of Scholarly Commons. For more information, please contact commons@erau.edu.

SHAPE OPTIMIZATION OF MICROFIBER
COMPOSITE ENERGY HARVESTERS

By

Suyash Lahoti

A Thesis Submitted to the Faculty of Embry-Riddle Aeronautical University
In Partial Fulfillment of the Requirements for the Degree of
Master of Science in Aerospace Engineering

May 2020

Embry-Riddle Aeronautical University

Daytona Beach, Florida

SHAPE OPTIMIZATION OF MICROFIBER
COMPOSITE ENERGY HARVESTERS

By

Suyash Lahoti

This Thesis was prepared under the direction of the candidate's Committee Chair, Dr. Mandar Kulkarni, Department of Aerospace Engineering, and has been approved by the members of the Thesis Committee. It was submitted to the Office of the Senior Vice President for Academic Affairs and Provost, and was accepted in the partial fulfillment of the requirements for the Degree of Master of Science in Aerospace Engineering.

THESIS COMMITTEE



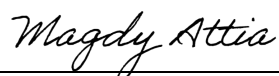
Chairman, Dr. Mandar Kulkarni



Member, Dr. Daewon Kim



Member, Dr. Sirish Namilae



Graduate Program Coordinator,
Dr. Magdy Attia

6/9/2020

Date



Dean of the College of Engineering,
Dr. Maj Mirmirani

6/9/2020

Date



Associate Provost of Academic Support,
Dr. Christopher Grant

6/9/2020

Date

ACKNOWLEDGMENTS

First and foremost, I would like to offer my utmost respect and gratitude to my advisor Dr. Mandar Kulkarni whose guidance and supervision has helped me achieve my goals. His knowledge and continued support were great assets to have on this challenging journey. His door was always open for questions which were challenging and even silly sometimes, and there was never any judgement which helped boost my confidence. Without his constant help, I don't think I would be able to push myself to achieve my goals.

I would also like to thank my committee members, Dr. Daewon Kim who let me use the Structures lab in the Lehman building which not only served as an office space for me but also where I was able to use his equipment's to perform the necessary experiments in order to complete this research. Also, Dr. Sirish Namilae who had given me insightful suggestion for my research. The physical and technical contribution of Embry-Riddle Aeronautical University is truly appreciated. Without their funding and support, this research couldn't have been completed.

I must also express my profound gratitude to my parents, Vikram Lahoti and Rina Lahoti without whom all this would not be possible. They always encouraged me to do my best and had an unconditional faith in me.

Lastly, I would like to thank my friends: Sarath, Mansi, Omkar, Madhur, Yamini, Ravi, Simon, Jason and Zheenan who were always there to cheer me up whenever I was feeling low. Thank you.

ABSTRACT

A model of energy harvesting beam with a piezoelectric material, microfiber composite (MFC), in a unimorph configuration was setup in Matlab using the governing equations of motions of a coupled electromechanical system. The equations of motion were derived using Hamilton's variational principles and constitutive relations of a piezoelectric material. The mathematical model developed in Matlab was validated with an experiment and frequency response functions. The validated model was used to perform shape optimization so as to obtain the shape of the beam and the patch that harvests the largest voltage. The shape variables were length of the beam (L_B), length of the patch (L_P), and width of the beam. Optimization reveals that voltage increases with length of the beam and with an inverse tapering (increasing width) of the beam from the root to the tip. This approach presents a systematic way to design energy harvesters and can serve as the basis for the conceptual design of energy harvester for applications such as morphing wings, smart shoe, MEMS devices, etc.

TABLE OF CONTENTS

ACKNOWLEDGEMENTS.....	iii
ABSTRACT.....	iv
LIST OF FIGURES.....	vii
LIST OF TABLES.....	x
SYMBOLS.....	xi
1. Introduction.....	1
1.1. Background.....	1
1.2. Motivation and Thesis Statement.....	3
1.3. Intellectual Merit.....	4
1.4. Thesis Flow and Outline.....	5
1.5. Piezoelectric Materials.....	6
1.6. Literature Survey of Modelling of Energy Harvesters.....	12
1.7. Literature Survey About Optimization of Energy Harvesters.....	15
2. Model for Energy Harvester.....	19
2.1. First Assumption.....	22
2.2. Second Assumption.....	26
2.3. Third Assumption.....	27
2.4. Compact Equation for Energy Harvester Model.....	27
2.5. Implementation of a Varying Cross-Section of the Energy Harvester Model..	30
3. Model Validation.....	34
3.1. System Identification Experiment.....	34
3.2. Energy Harvester Experiments.....	42
3.3. Inputs for Matlab Model.....	45
3.4. Results and Discussion.....	49
3.5. Conclusion.....	52
4. Optimization.....	53
4.1. Sensitivity Analysis.....	53
4.1.1. Finite Difference Method.....	55
4.1.2. Complex Step.....	56
4.1.3. Discrete Analytical.....	57
4.1.4. Exact or Analytical.....	57
4.2. Two Variable Optimization.....	59
4.2.1. Length of Beam and Length of Patch Case.....	60
4.2.2. Length of Beam and Delta (δ) Case.....	66
4.3. Three Variable Optimization.....	72
4.4. Conclusion.....	77

5. Conclusions, Recommendations and Future Work.....	80
5.1. Conclusion.....	80
5.2. Knowledge Gained and Challenges Tackled.....	82
5.3. Recommendations and Future Work.....	83
REFERENCES.....	85
APPENDIX A.....	88

LIST OF FIGURES

Figure	Page
1.1 Concept of smart shoe harvester (Meier et al., 2014).....	2
1.2 Flow process of thesis.....	3
1.3 Inputs for mathematical model (left) and experimental setup for the energy harvester (right).....	4
1.4 Working mechanism of piezoelectric energy harvester (Ali & Ibrahim, 2012).....	7
1.5 Dipole arrangement before and after application of an electrical potential (Hook & Hall, 2010).....	9
1.6 ‘d33’ mode and ‘d31’ modes (Kubba & Jiang, 2014).....	9
1.7 Unimorph versus bimorph configuration.....	10
1.8 Layers of a MFC (Kovalovs et al., 2007).....	10
1.9 Concept of morphing wings using MFC (Ohanian et al., 2012).....	12
2.1 First four modes of the energy harvester cantilever beam.....	26
2.2 Energy harvester beam schematic.....	27
2.3 Variation of width with delta (δ).....	32
2.4 Different parameters of the energy harvester beam.....	32
2.5 Mode shapes for a cantilever beam for different values of delta (δ).....	33
3.1 Vibration test using shaker (Model Shop Inc).....	36
3.2 Impact hammer test (Model Shop Inc).....	36
3.3 Tektronix function generator (AFG 3051C) and Brüel and Kjær power amplifier (Type 2718).....	38
3.4 Glass fiber beam with MFC (M8528P2) patch and PCB accelerometers.....	38
3.5 PCB signal conditioner (Model 482C) and National Instruments DAQ (NI 9174).....	39

Figure	Page
3.6 Sample input and output recorded from the transducers.....	40
3.7 Frequency response functions generated using bodeplot for one set of recorded data.....	40
3.8 Worst (top) and best (bottom) fits between the state space and experimental data.....	41
3.9 Variable resistance module from Smart Materials Corp.....	43
3.10 Experimental flow diagram.....	44
3.11 Beam setup for energy harvester experiment with accelerometer at base.....	44
3.12 Different inputs needed for voltage from Matlab model.....	47
3.13 Inputs for mass, stiffness, electromechanical coupling matrices and capacitance term.....	47
3.14 Terms obtained from experiment.....	48
3.15 Voltage output from Matlab model and experiment.....	49
3.16 Variation of frequency at which peak power is obtained at different values of resistance (Liao & Sodano, 2008).....	51
3.17 Variation of tip displacement versus frequency for different resistance (Junior et al., 2009).....	52
4.1 Flowchart of different sensitivity analysis methods.....	54
4.2 Plot of log of step size versus log of error.....	56
4.3 Cantilever beam setup and beam cross section.....	58
4.4 Different design variables for the shape optimization problem.....	60
4.5 Design space for length of the beam (L_B) and length of the patch (L_P).....	62
4.6 Optimization paths for L_B and L_P case.....	63
4.7 Iteration versus objective function for the L_B and L_P case.....	64

Figure	Page
4.8 Iterations versus first order optimality for L_B and L_P case.....	64
4.9 Design space for length of the beam (L_B) and width variation parameter (δ).....	68
4.10 Optimization paths for the L_B and δ case.....	69
4.11 Iterations versus objective function for the L_B and δ case.....	70
4.12 Iterations versus first order optimality for L_B and δ case.....	70
4.13 Optimization path for the three design variable case.....	74
4.14 Iterations versus objective function for the three design variable case.....	75
4.15 First order optimality for the three design variable case.....	75
4.16 Final optimization shapes for the different cases.....	78

LIST OF TABLES

Table	Page
2.1 Roots for the characteristic equation of a cantilever beam.....	26
3.1 List of properties of the MFC patch.....	45
3.2 List of properties of the glass fiber composite beam.....	45
3.3 Voltage obtained from mathematical model and experiment at different frequencies.....	50
4.1 Properties and dimensions of the cantilever beam	58
4.2 Comparison of frequency sensitivity using different methods.....	59
4.3 Iterations and values of L_B and L_P for the active-set algorithm.....	65
4.4 Iterations and values of L_B and L_P for the SQP algorithm.....	65
4.5 Iterations and values of L_B and L_P for the interior-point algorithm.....	66
4.6 Iterations and values of L_B and δ for the active-set algorithm.....	71
4.7 Iterations and values of L_B and δ for the SQP algorithm.....	71
4.8 Iterations and values of L_B and δ for the interior-point algorithm.....	72
4.9 Iterations and values of L_B , L_P and δ for the active-set algorithm.....	76
4.10 Iterations and values of L_B , L_P and δ for the SQP algorithm.....	76
4.11 Iterations and values of L_B , L_P and δ for the interior-point algorithm.....	77

SYMBOLS

K	Kinetic energy
U	Potential energy
$\int f \delta x$	External work done to the system
S	Strain
T	Strain
D	Electrical Displacement
V	Volume
E	Applied electric field
v	Velocity
u	Mechanical Displacement
x	Position along the beam
q	Charge
ρ	Density
f	Applied force
nf	Number of modes used
b	Beam material
p	Piezoelectric material
c	Young's modulus
$()^S$	Constant strain
$()^E$	Constant electric field
e	Piezoelectric coupling coefficient
d	Coupling coefficient

δU	Variation of potential energy
δK	Variation of kinetic energy
ϕ	Assumed mode shape
$r(t)$	Temporal co-ordinates
E	Young's modulus
I	Moment of inertia
A	Area of cross section
ω_n	Natural frequency of beam
L	Length of beam
$\beta_n L$	Characteristic roots
t_p	Thickness of patch
t_B	Thickness of beam
M_B	Mass matrix of beam
M_p	Mass matrix of patch
C	Damping matrix
Θ	Electromechanical coupling term
C_p	Capacitance term
L_B	Length of beam
L_p	Length of patch
w_B	Width of beam
w_p	Width of patch
c_B	Young's modulus of beam
c_p	Young's modulus of patch

d_{31}	Piezoelectric coefficient
K_{33}	Dielectric constant
y	Thickness function
R	Resistance
F	Force term
ω_f	Forcing frequency
A_0	Amplitude of base displacement
w_{B0}	Width of beam at clamped end
δ	Width variation parameter
$H(j\omega)$	Frequency response function
X	Phasor of input
Y	Phasor of output
a	Amplitude of base acceleration
ζ	Damping ratio

1. Introduction

In this chapter discussion will be made in the background of energy harvesters, the motivation behind this research, flow of this thesis, intellectual merit and literature review. The literature review will consists of two sections one for the energy harvesting related research and the other for the optimization of the energy harvested.

1.1. Background

Over the past two decades, there has been a tremendous amount of research dedicated to energy harvesting. Energy harvesting can be defined as a process of capturing the ambient waste energy and utilizing it for some other applications like powering other devices such as batteries, MEMS, etc. This is mainly done so that we may optimize our resources and waste as little as possible, effectively saving both energy and money. A few sources of ambient energy from which energy harvesting is possible are wind, light, mechanical vibrations, etc. Out of the sources listed our focus will be on energy harvesting from mechanical vibrations. This will be done using smart materials which can be defined as materials that have one or more properties that can be significantly changed in a controlled fashion by an external stimulus such as stress, magnetic or electric field, temperature, etc.

Many different methods are available to obtain electrical energy from mechanical vibration (Anton & Sodano, 2007) some of which are electromagnetic induction, dielectric elastomers, electrostatic generation, and piezoelectric materials. Out of the listed methods, the most popular method is the energy conversion using piezoelectric materials. The reason for their popularity is because using such materials energy is directly converted from mechanical to electric and also they can be easily integrated into

any system. There are a wide variety of piezoelectric materials which suit different types of operating conditions.

Piezoelectric energy harvesting systems have a wide variety of applications ranging from human wearable devices, aerospace industry, civil infrastructure, biomedical devices, etc. An interesting application of these energy harvesters is in the form of a shoe harvester. A study was conducted by Shenck and Paradiso (2001) for harvesting the lost energy from a shoe by a using pre-stressed PZT uniform. This concept has caught the eyes of many researchers (Frontoni et al., 2013; Xu & Li, 2019). The concept involves placing the piezoelectric materials in the sole of the shoe and harvesting the energy while performing daily activities like walking, running, etc. The basic composition of a smart shoe is shown in Figure 1.1 (Meier et al., 2014).

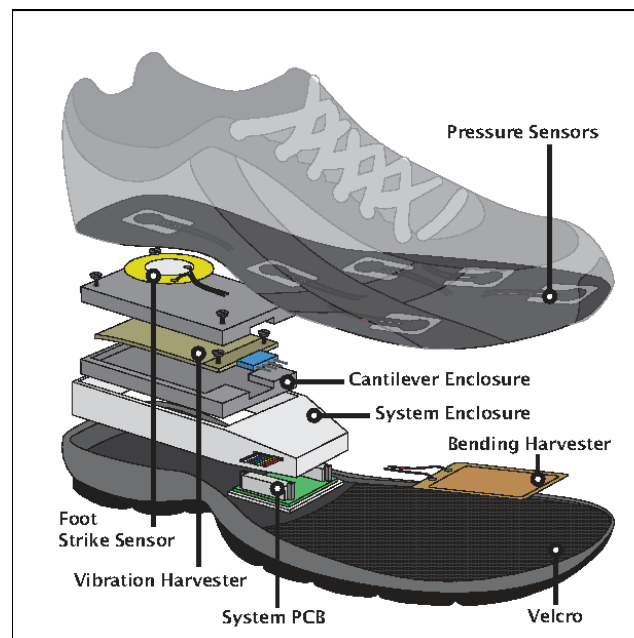


Figure 1.1 Concept of smart shoe harvester (Meier et al., 2014)

1.2. Motivation and Thesis Statement

The piezoelectric material that will be used in this research is a Microfiber Composite (MFC). A mathematical model of this energy harvester will be developed on Matlab using an electromechanical coupled governing equation. This mathematical model will be validated against an experiment by using the same conditions for both the experiment and the model. After the validation of the model, it will then be used to perform a shape optimization for maximizing the harvested voltage. The optimization will be gradient-based and will involve three shape variables. This can be used as a basis to perform 3-D optimization. The overall flow of this thesis is shown in Figure 1.2.

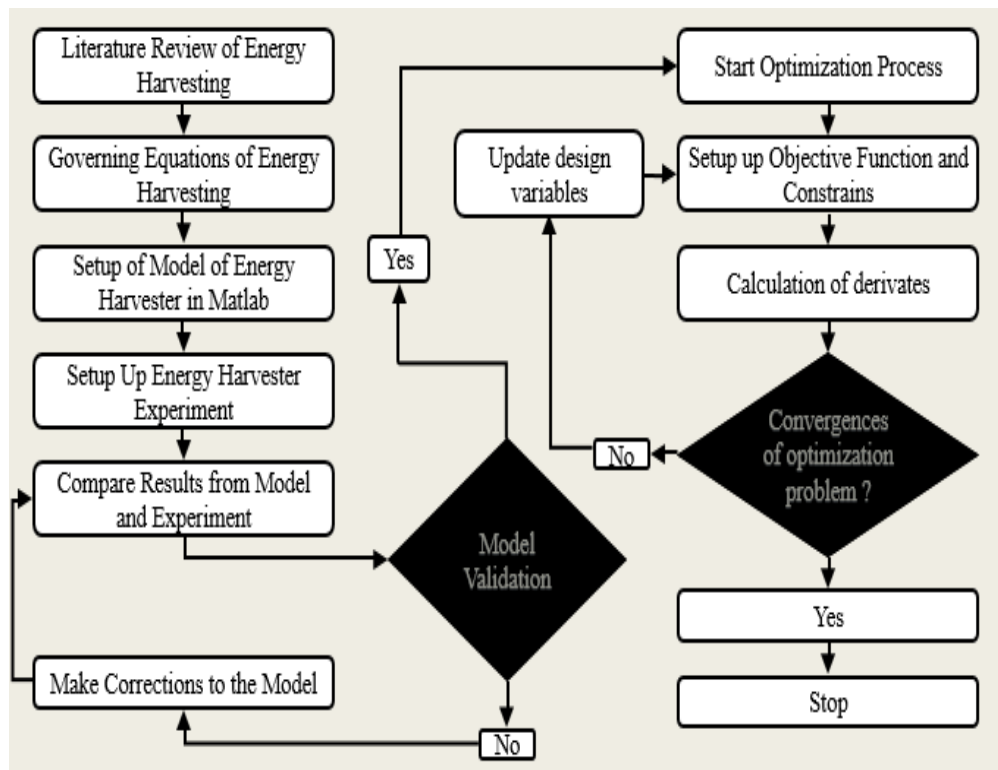


Figure 1.2 Flow process of thesis

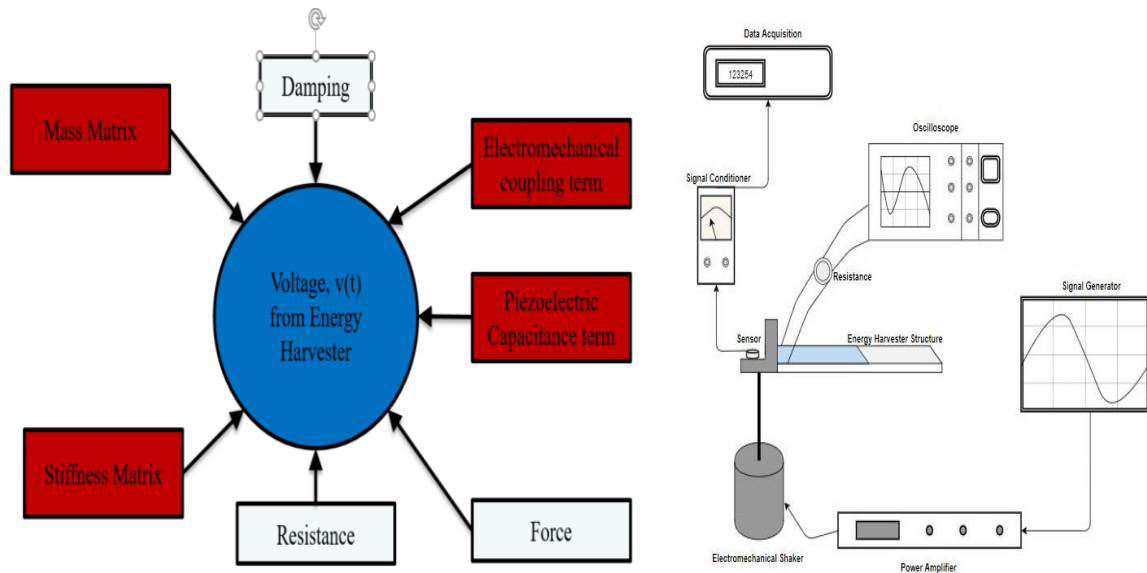


Figure 1.3 Inputs for mathematical model (left) and experimental setup for the energy harvester (right)

Figure 1.3 shows the different inputs that will be required to obtain the voltage from the mathematical model which will be developed in Matlab versus the experimental setup that will be used to validate the mathematical model developed. More details about the mathematical model and experiment will be discussed in Chapter 2 and Chapter 3 respectively. After the model validation is performed it will be used to perform the shape optimization of the energy harvester beam which will be discussed in Chapter 4.

1.3. Intellectual Merit

In this thesis following will be the intellectual merit or in other words the novelty of this thesis:

- Shape optimization will be performed on a unimorph type of configuration of an energy harvesting beam. Optimization has been performed for a bimorph configuration and researches have also studied optimization of the electrical parameters of an energy harvester, but up to the author's knowledge it hasn't been

performed on this type of configurations. Shape optimization is more challenging compared to size optimization and the results indicate that changing the length and width of the beam significantly help in generating more voltage from such energy harvesters.

- An exponentially varying width profile will be introduced. This would imply using different mode shape equations and also considering the effects of a varying cross section on the amount of energy harvested.
- Lastly, the formulation of optimization problem and setting up the problem in Matlab will be done in such a way that addition of multiple design variables is convenient. Addition of multiple design variables would aid in performing a more rigorous optimization problem and may give more design freedom.

1.4. Thesis Flow and Outline

Chapter 1 of this thesis will provide an understanding of piezoelectric materials and their properties which make them ideal for energy harvesting applications. Also in this chapter, a literature survey of energy harvester models will be provided along with work done on optimization of these energy harvesters.

Chapter 2 comprises of the derivation of the electromechanical coupled governing equation of motions based upon which a mathematical model will be set up in Matlab. The different inputs required to obtain the voltage from the model will be discussed.

Chapter 3 will discuss about experimental setup against which the mathematical model setup in Matlab will be validated against. In this chapter experimental setup for the parameter identification, namely the natural frequency of the cantilever beam will also be shown. Results from both experiments will be shown and discussed.

In Chapter 4, the optimization problem will be introduced. The discussion will include setting up of the objective function and constraints along with the design variables. The optimization will consist of two cases, a two-design variable case, and a three design variable case, while the objective function will be the same for both the cases. The obstacles and challenges for the optimization process will also be given. Results from the optimization will also be shown. Lastly in Chapter 5 a conclusion of this thesis will be provided along with future work that can be done in to improve the results to achieve even higher accuracy.

1.5. Piezoelectric Materials

Smart Material can be defined as materials that have one or more properties that can be significantly changed in a controlled fashion by an external stimulus such as stress, magnetic or electric field, light, pH, temperature, etc. These materials have a wide range of applications, including sensors, actuators, energy harvesters, artificial muscles, etc. Some of the types of smart materials are piezoelectric, shape-memory, electroactive polymers, ferrofluids, etc. In this thesis, a piezoelectric type of smart material will be used for energy harvesting application.

The piezoelectric effects were studied by several researchers in the 18th Century but the effect was first demonstrated by Jacques and Pierre Curie in 1880's. They realized this effect when certain crystals that were subjected to mechanical force became electrically polarized.

For the past two decades, vibration-based energy harvesting systems have been studied to understand their application in self-powered systems (Aridogan et al., 2014). With such self-powering systems the need for an external power source for their

operation is eliminated. This not only saves cost for the battery and other electrical circuitry involved but also reduced the weight and complexity of the systems, which gives way for much lighter systems which are very advantageous.

A basic working mechanism for a piezoelectric based energy harvester can be illustrated from Figure 1.4 (Ali & Ibrahim, 2012). It usually involves the conversion of kinetic energy from the vibrations to electric energy. The strain produced due to vibrations is responsible for the generation of electric potential in such piezoelectric materials. The configuration usually involves a cantilever beam which is subjected to either base excitation or a load at the tip. This load or excitation vibrates the structures, inducing strain on the structure causing it to vibrate and hence producing an electrical potential that can be read on a device such as an oscilloscope, could be stored or used to power certain devices.

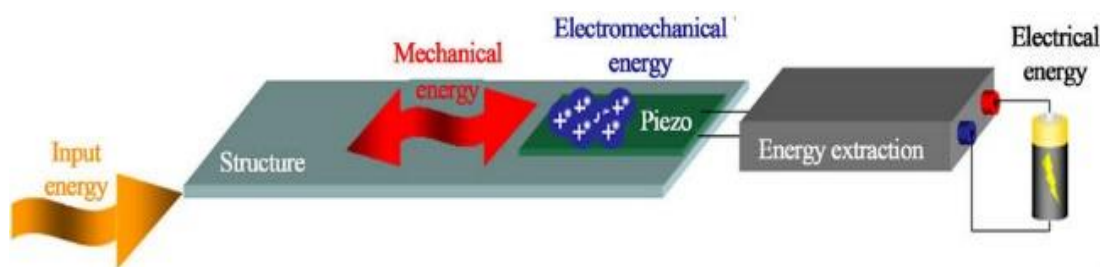


Figure 1.4 Working mechanism of piezoelectric energy harvester (Ali & Ibrahim, 2012)

Piezoelectric energy harvesters have been extensively in powering microelectromechanical systems (MEMS) (Beeby et al., 2006; Sodano et al., 2004; Saadon & Sidek, 2011). The reason they are so popular for MEMS is that the amount of energy harvested from piezoelectric materials is quite small and hence cannot be used for larger applications. In this thesis, a mathematical model of an electromechanical system

will be developed based on the findings of the above authors. A brief description of the fundamentals of power harvesting from piezoelectric materials is given below.

The piezoelectric effect can be broadly classified into two domains: the direct effect Equation 1 and the indirect effect Equation 2 (Tichý et al., 2010). The direct effects states that any mechanical strain applied to the system is converted into electrical charge. The indirect states that an electrical potential applied to the system is converted into a mechanical strain. The direct effect is the one responsible for the energy harvesting properties of piezoelectric materials.

$$\{D\} = [e]^T \{S\} + [\epsilon] \{E\} \quad (1)$$

$$\{T\} = [c]^E \{S\} - [e] \{E\} \quad (2)$$

Crystalline materials are solid materials that are made up of crystals (Hook & Hall, 2010). Piezoelectric materials are also crystalline materials made up of ions or molecules. At temperatures below the Curie temperature, the lattice structure of the crystals becomes deformed and asymmetric. This causes the formation of dipoles that are randomly oriented. Application of an electrical potential causes these dipoles to be oriented in a particular direction (depending upon the electrical potential) hence causing them to contract or expand. This is illustrated in Figure 1.5.

Piezoelectric materials also have another type of operation mode known as the coupling mode of operation. This mode of operation depends mainly on the direction of polarization. To get a better understanding of the direction of polarization consider Figure 1.6. As seen in Figure 1.6 there exists three directions in any cubic lattice, 1 along the length, 2 along the width and 3 across the thickness. The two modes called the ‘d31’ mode and ‘d33’ mode (Kubba & Jiang, 2014) are quite self-explanatory, where ‘d31’

means that the poling is across the '3' direction or thickness and the strain is measured along '1' direction while 'd33' modes stands for poling along '3' and measurement along '3' as well. The 'd31' mode is the one responsible for energy harvesting applications.

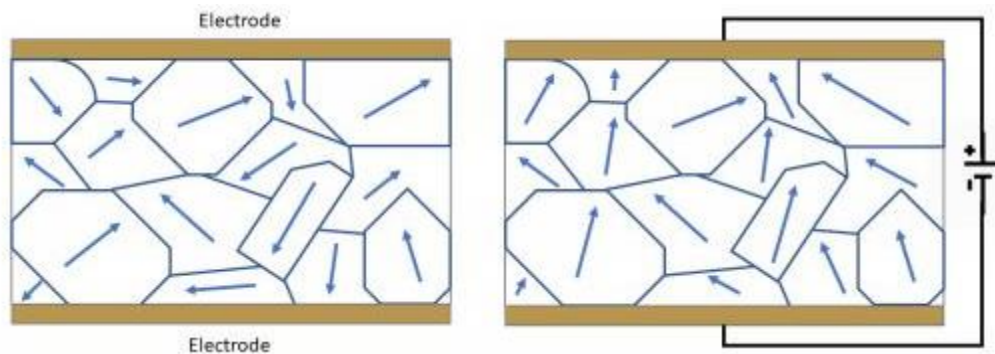


Figure 1.5 Dipole arrangement before and after application of an electrical potential (Hook & Hall, 2010)

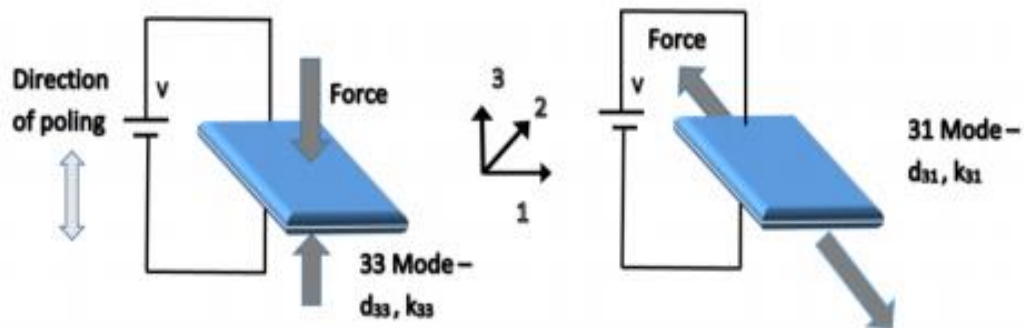


Figure 1.6 'd33' mode and 'd31' mode (Kubba & Jiang, 2014)

Piezoelectric materials configuration can be broadly classified into two: unimorph and bimorph. A unimorph configuration is generally a single piezoelectric layer on an elastic substrate (usually a thin metal) while a bimorph configuration involves sandwiching an elastic substrate between two piezoelectric layers. Either of these

configurations is used for energy harvesting study and application (Dow et al., 2014). These configurations are shown in Figure 1.7.



Figure 1.7 Unimorph versus bimorph configuration

There are many different types of piezoelectric materials that are available to be used for energy harvesting applications. Some of them are Lead Zirconate Titanate (PZT), Polyvinylidene Fluoride (PVDF), Microfiber Composite (MFC), etc. As already mentioned MFC will be used for energy harvesting applications in this study.

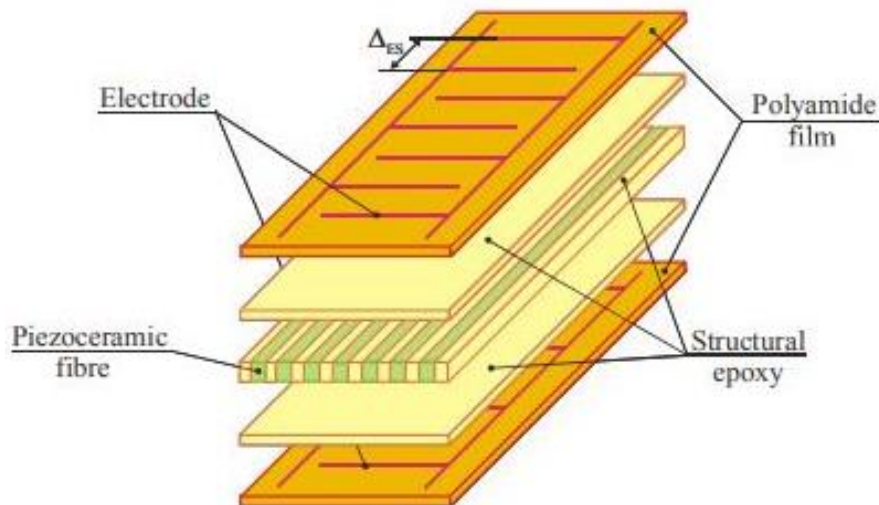


Figure 1.8 Layers of a MFC (Kovalovs et al., 2007)

Microfiber composite (MFC) was invented by NASA in 1999 (Smart Materials Corp) at NASA's Langley Research Center in Hampton, Virginia (Kovalovs et al., 2007). It

consists of rectangular piezo ceramic rods that are sandwiched between layers consisting of electrodes, polyimide films and adhesive shown in Figure 1.8. Though PZT has higher energy harvesting properties compared to MFC (Shen et al., 2003), MFC's are extremely flexible, durable and can conform to any surface which makes it a better candidate for vibration-based energy harvesting applications.

High (2003) published an extremely detailed manual for the manufacturing of MFC. MFC's generally have a uniform geometry which includes the electrode spacing and PZT rods and also avoid air voids or any other particulate inclusion. Higher efficiency of electric field transfer to the rods can be directly related to the rectangular shape of the rods which promotes an improved contact between the adjacent electrode and the piezo ceramic rods.

In the aerospace industry, an interesting application for MFC materials is a morphing wing. Although in the current scenario the shape of wings of an airplane is fixed, morphing wings would innovate the industry as it would lead to better efficiency and flight control. The concept involves using MFC patches on the wing of an aircraft, whereby supplying an electrical potential to those patches, causes a change in the shape of the patch and thus the shape of the wing can be changed to perform aircraft control operations. The design and working of such a wing is shown in Figure 1.9 (Ohanian et al., 2012).

Though the above is an extremely interesting and innovative concept and has a very practical application in the real world it is still a topic under research. In this study, contributions would be made towards obtaining the best shape of the MFC patch so that

the maximum output is achieved from them. This could help in better actuation and also may help to reduce a small percentage of weight since an optimized shape could be used.

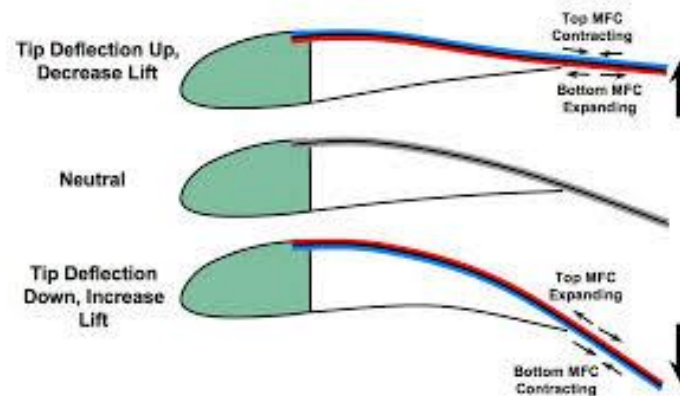


Figure 1.9 Concept of morphing wings using MFC (Ohanian et al., 2012)

1.6. Literature Survey of Modelling of Energy Harvesters

As discussed in the previous section piezoelectric materials have a very high potential to be used in vibration-based energy harvesting applications. In this section, we discuss about the research that has been made towards modeling of these harvesters. Based on the research done on this subject a mathematical model was developed, as explained in Chapter 2 of this Thesis.

The first study done towards developing a model of these electromechanical coupled systems was by Hagood et al. (1990). Though the study was not aimed towards developing a model for energy harvesters it formed the base for all other studies. They used generalized Hamilton's principle of variation energy to derive an electromechanical coupled governing equation of motion for sensor and actuator applications of these piezoelectric materials.

Early work done in the modeling of such electromechanical systems was by Crawley and Anderson (1990). A comparison of a uniform strain model, Bernoulli-Euler model, and a finite element model was made for induced strain actuation. Since the Bernoulli-Euler model predicted the most accurate results for extensional and bending deformations it was used to develop actuation equations for PZT devices.

Another early study by Umeda et al. (1996) investigated the effect of a power generated by a plate with a piezoceramic wafer by impacting the plate with a free-falling ball made up of steel. To simulate the generated energy an electrical equivalence model was used. Electric power generated from the mechanical impact using the PZT was also calculated. The model was mainly used to determine the maximum efficiency of the conversion from mechanical to electrical energy.

Modeling of energy harvesters from piezoelectric materials was first discussed by Sodano et al. (2004). The same Hamilton's principle and piezoelectric governing equations were used to develop a coupled equation of motion for Quick Pack type of piezoelectric material. An important addition in this research compared to the previously published one was the addition of material damping to the derivation. The first four modes of vibration of a cantilever beam were used to validate the mathematical model developed against the experiment. An excellent validation of their mathematical model was obtained from their experiments.

Song et al. (2007) also developed a similar electromechanical coupled equation of motion for an energy harvesting system by using an MFC patch. This was also based upon Hamilton's principle but in this study, only the first mode of vibration was used for the model validation. They achieved good results and also discussed series and parallel

connections for the energy harvester model. It was also observed that the highest energy output was achieved around the first natural bending frequency of the system.

Liao and Sodano (2008) researched the accuracy of the single-mode energy harvester system by using the same approaches as the previously discussed papers. It was observed that a single-mode energy harvester was accurate enough to use for the model development. Based on their single-mode model, they developed an expression to determine the optimal resistance and electromechanical coupling coefficient. Using these expressions they determined the optimal resistance value for their model and also how resistance affected the power generated. Similar studies were also performed for the electromechanical coupling coefficient effect on power. The relation between electromechanical coupling and dielectric permittivity were also researched.

Abdelkefi et al. (2011) used Hamilton's principle and Euler-Bernoulli beam theory to derive the piezoelectric energy harvester cantilever beam equation of motion but also included coupled bending-torsion vibration to account for structures having tip mass on them. Natural frequency and mode shapes were validated with a model developed on a FEM software. They also developed a reduced-order model by using the Galerkin procedure. It was observed that the harvester's performance was increased by increasing the asymmetry of the structure.

A different approach to model these energy harvesters is also researched by Erturk and Inman (2008). A distributed parameter approach was used to develop the electromechanical model. Euler-Bernoulli beam assumption was the base for the model development. Along with beam bending, superimposed small rotations were also taken

into account while deriving the governing equations. Frequency response functions (FRF's) were used to validate the model and good co-relation was overserved.

In this thesis, the mathematical model formulation of the energy harvester beam will be based upon the equations formed by previous stated researches (Crawley & Anderson, 1990; Hagood et al., 1990; Liao & Sodano, 2008; Sodano et al., 2004; Song et al., 2007). Most of the terms explain in all the previously stated studies are the same with slight changes in each depending upon their criteria. Also, the experimental setup used by each of the previously stated studied in this section is the same and hence a similar experimental setup will also be used in this research.

1.7. Literature Survey About Optimization of Energy Harvesters

In the previous section, we discussed the different researches done on the modeling of the energy harvester system using both a mathematical model and a FEM model. These models were validated with experiments. After the validation of such models, the focus of the research shifted towards the optimization of these models to obtain the maximum energy. This could be achieved by either performing a structural optimization or optimization of the electric aspect of these energy harvesters. In this section, we will discuss the different studies performed in that aspect.

Yang et al. (2009) developed a FE model and simulated the energy stored on a capacitor using electronic design automation (EDA) software for an energy harvester system using one P1-type MFC and two P2-type MFC patches. They validated the model with an experiment for different configurations and were able to obtain good co-relation. They then used the FE model to optimize the performance of the energy harvesting system by performing a parametric study on the dimensions of the beam. Mainly the

thickness and length of the beam were varied and the effect on the voltage was observed. It was observed that by using a thicker and short beam the average voltage increased.

Gonzalez et al. (2010) studied the optimization from the electric system point of view of the energy harvester. They used a two-port network model and resistive load for the optimization by using a genetic algorithm. It was concluded from their research that a genetic algorithm would serve as a good tool to obtain an increased performance for such electromechanical coupled systems.

Ottman et al. (2002) also looked into the electrical circuitry for the optimization for these energy harvester systems. They developed an adaptive approach for the optimization by using a step down dc-dc converter. An expression for the duty cycle-power relationship was also formulated. The expression for the duty cycle was validated against an experiment. A trend was observed whereupon increasing the mechanical excitation the duty cycle would tend to reach a constant value.

Friswell and Adhikari (2010) performed a detailed parametric study on the sensor shape design for cantilevered piezoelectric beams for energy harvesting applications. They developed mass and stiffness matrices for finite element analysis using Euler-Bernoulli beam elements. In order to be consistent with a FE model all the terms necessary to obtain the power were also in matrix form. Once the model was developed optimization was performed to increase the power output. The model developed in this study was a multiple mode model that made the matrices for each term an n by n matrix (where n is the number of modes used) making the optimization complex. Hence the study shifted towards a parametric study for different shapes of the sensor on the cantilever beam. Four shapes of sensors were investigated namely uniform, triangular,

smooth segment, and square segments. It was observed that segmented shapes (square and smooth) obtained the most power while the least was observed in the uniform shape.

The first research performed towards shape optimization of energy harvester systems was the one by Dietl and Garcia (2010). They also developed an electromechanical model by using Hamilton's varying principle but the novelty of this work was the inclusion of varying width in the derivation of the terms of the equation of motion. They later used these sets of equation to perform a shape optimization of the systems to maximize the energy output and also study the effect of base excitation on the harvester energy. Using a linear width profile three beam shapes were studied namely, rectangular, linear taper and reverse taper. The optimization achieved a 0.52% increase in performance with the shape tending towards the reverse taper. They also studied the effect of tip mass to beam mass ratio but no optimization was performed in this aspect.

Another research by Tabatabaei et al. (2016) performed a multi-objective shape optimization using an artificial immune system for the design of piezoelectric energy harvesting systems. Similar to most of the other research in the modeling aspect Euler-Bernoulli/ Rayleigh-Ritz method was used to model both unimorph and bimorph configurations. The model included varying width for performing the shape optimization. The optimization was performed using an AIS tool which was the novelty of this research. The optimized model took the shapes similar to a reverse cantilever i.e. increasing width from the cantilever end towards the free end.

For this thesis comparison of the optimization could be made against studied performed by researches stated in this section (Dietl & Garcia, 2010; Friswell & Adhikari, 2010; Tabatabaei et al., 2016) since all of them performed either a parametric

study or optimization for the shape design variables and how they affected the final power output or voltage. The same is the goal of this study where optimization will be performed on the shape design variables to see what effect they have on the output voltage or power.

2. Model for Energy Harvester

In this section, we will discuss the derivation of governing equations of motion in order to set up the mathematical model for the electromechanical coupled system of piezoelectric materials. This model was set up in Matlab. The different inputs needed and the process of deriving/ obtaining these will also be discussed in this section. The final output of the model will be the voltage generated by the piezoelectric material (MFC patch in this case). The model was validated with an experimental setup.

From the previous section, it can be concluded that piezoelectric materials are being used for powering MEMS and wireless devices, and also for storing energy in batteries. Developing a model of these piezoelectric materials is extremely important since it can give us an idea of how much power or energy can be obtained from these devices. With the help of the developed model, devices can be manufactured with the necessary electrical equipment needed to handle these energies. Also a mathematical model will make way for performing optimization in the order to utilize the resource in the maximum way possible.

It has been seen the most of the mathematical models developed have been for a cantilever beam type of configuration. The piezoelectric configuration could be either a bimorph type or a unimorph type as shown in Figure 1.7. Although the configurations are slightly different the model developed can be used for either configuration with a small change in certain parameters.

The model developed by Hagood et al. (1990) has been used as a base for most of the energy harvester models developed till now and will also be used as a base in this thesis. The additions provided by Sodano et al. (2004) will also be incorporated when deriving

the model. Lastly, the equation for the final energy output in this thesis will be the same as the one provided by Song et al. (2007) since this is based on a single-mode of vibration. The single-mode model makes the optimization process easier compared to a multiple mode model, also it can be seen the single-mode model is accurate enough to depict the behavior of the energy harvester system.

Energy methods will be used in this section in to develop the mathematical model for a unimorph piezoelectric cantilever beam configuration. Hamilton's Principle will be used as a starting point for the derivation, which states that the variation indicator at all times must be zero as shown in Equation 3 described by researches (Hagood et al., 1990; Sodano et al., 2004).

$$\delta \int_{t_1}^{t_2} [\delta K - \delta U + f\delta x] dt = 0 \quad (3)$$

Where K, U and $f\delta x$ terms can be defined by the following set of equations,

$$K = \frac{1}{2} \left(\int_{V_B} \rho_B v^T v dV_B + \int_{V_P} \rho_P v^T v dV_P \right) \quad (4)$$

$$U = \frac{1}{2} \left(\int_{V_B} S^T T dV_B + \int_{V_P} S^T T dV_P \right) - \int_{V_P} E^T D dV_P \quad (5)$$

$$f\delta x = \sum_{i=1}^{nf} \delta u(x_i) \cdot f_i(x_i) - \sum_{j=1}^{nq} \delta vol \cdot q_j \quad (6)$$

In Equation 4, 5, and 6, K, U and $f\delta x$ represent kinetic energy, potential energy and external work done to the system respectively. S is the strain, T is the stress, D is the electrical displacement, V is the volume, E is the applied electric field, v is the velocity, u represents the displacement, position along the beam is represented by x, vol represents the applied voltage, q is the charge, ρ is the density, f is the applied force, nf and nq are summations for the number of modes used and the subscripts b and p represent the beam

and piezoelectric material respectively. Equation 6 consists of two terms, the first term which is the summation of the dot product of u and f is the mechanical work done on the system and the other term is the applied electrical work. To derive the equation of motion of such an electromechanical coupled system from the previously described set of equations it is important to introduce the piezoelectric constitutive equations. This is done so that they can be substituted in the kinetic and potential energy equations to obtain the correct terms. The piezoelectric equations to be introduced initially are,

$$[T] = c^E S - e^T E \quad (7)$$

$$[D] = e S + \epsilon^S E \quad (8)$$

In Equations 7 and 8 ϵ is the dielectric constant, c is Young's modulus, superscripts $()^S$ and $()^E$ indicate that the parameters were measured at constant strain and constant electric field. These equations describe the relationship between the electric and mechanical properties of any piezoelectric material. These relations are responsible for the electromechanical coupling of an energy harvester system and hence need to be included in the mathematical model. The stress and electric field are related by the term e which is called the piezoelectric coupling coefficient and is represented as shown in Equation 9.

$$e = d_{ij} c^E \quad (9)$$

The coupling coefficient is generally represented by the term d , where the subscript i represents the direction of the electric field applied and j represents the poling direction. Substituting Equations 7 and 8 in the potential energy term U , Equation 5 is transformed

into Equation 10. Using Equation 10 and Equation 4 we obtain the variation of potential energy and kinetic energy as shown in Equations 11 and 12 respectively.

$$U = \frac{1}{2} \left(\int_{V_B} S^T c_B S dV_B + \int_{V_P} S^T c^E S dV_P - \int_{V_P} S^T e^T E dV_P - \int_{V_P} E^T e S dV_P - \int_{V_P} E^T \epsilon^S E dV_P \right) \quad (10)$$

$$\delta U = \int_{V_B} \delta S^T c_B S dV_B + \int_{V_P} (\delta S^T c^E S - \delta S^T e^T E - \delta E^T e S - \delta E^T \epsilon^S E) dV_P \quad (11)$$

$$\delta K = \int_{V_B} \rho_B (\delta v^T) v dV_B + \int_{V_P} \rho_P (\delta v^T) v dV_P \quad (12)$$

Combing Equations 10, 11 and 12 and substituting in Equation 3 we obtain the equation below,

$$\int_{t_1}^{t_2} \left[\int_{V_B} \rho_B (\delta v^T) v dV_B + \int_{V_P} \rho_P (\delta v^T) v dV_P - \int_{V_B} \delta S^T c_B S dV_B + \int_{V_P} (\delta S^T c^E S - \delta S^T e^T E - \delta E^T e S - \delta E^T \epsilon^S E) dV_P - \sum_{i=1}^{nf} \delta u(x_i) \cdot \phi_i(x_i) - \sum_{j=1}^{nq} \delta vol. q_j \right] \quad (13)$$

Equations of motion of any electromechanical system containing piezoelectric materials can be solved for using equation. Some of the assumptions to solve Equation 13 is given below.

2.1. First Assumption

The first assumption made is that the displacement of the beam is written in the form of summation of assumed mode shape and temporal co-ordinates which is a standard Rayleigh-Ritz procedure and is represented mathematically as shown below. In

Equation 14 ϕ_i is the assumed mode shapes which can be set to satisfy any combination of boundary conditions, $r_i(t)$ is the temporal coordinate of the displacement and the number of modes used in the analysis is represented by N. In this thesis a cantilever beam will be used in the developed of the mathematical model. To derive the equation for the mode shape of a cantilever beam we start with the equation for free vibrations of an Euler-Bernoulli beam:

$$u(x,t) = \sum_{i=1}^N \phi_i(x) r_i(t) \quad (14)$$

$$EI \frac{\partial^4 u(x,t)}{\partial x^4} = -\rho A \frac{\partial^2 u(x,t)}{\partial t^2} \quad (15)$$

$$u(x,t) = X(x)Z(t) \quad (16)$$

$$\frac{EI}{\rho A X(x)} \frac{\partial^4 (X(x))}{\partial x^4} = -\frac{1}{Z(t)} \frac{\partial^2 Z(t)}{\partial t^2} \quad (17)$$

Where E is Young's modulus, I is the moment of inertia, ρ is density and A is the area of cross-section. Equation 15 is best solved by the separation of variable technique, which states that the equation can be separated into two parts, one for the position and the other for the time. Substituting Equation 16 into Equation 15 and dividing by $\rho A X(x) Z(t)$ we get Equation 17.

From Equation 17 it is seen that the left-hand side doesn't vary with time (t) and hence right side must be a constant. Vice-versa can also be concluded since the right-hand side doesn't vary with position (x). Since each side is a constant, Equation 16 is valid and the method of separation of variables can be used. Let us introduce a constant

ω_n^2 which is a real quantity and ω_n represents the natural frequency of the beam. Re-writing, we get two differential equation,

$$\frac{\partial^4 X}{\partial x^4} - \beta_n^4 X = 0 ; \frac{\partial^2 Z}{\partial t^2} + \omega_n^2 Z = 0 \quad (18)$$

where,

$$\beta^4 = \frac{\omega_n^2 \rho A}{EI} \quad (19)$$

$$u(0,t) = X(0) ; \frac{\partial u(0,t)}{\partial x} = \frac{\partial X(0)}{\partial x} = 0 \quad (20)$$

$$\frac{\partial^2 u(L,t)}{\partial x^2} = \frac{\partial^2 X(L)}{\partial x^2} = 0 ; \frac{\partial^3 u(L,t)}{\partial x^3} = \frac{\partial^3 X(L)}{\partial x^3} = 0 \quad (21)$$

$$X(x) = C_1[\cos(\beta_n x) + \cosh(\beta_n x)] + C_2[\cos(\beta_n x) - \cosh(\beta_n x)] \\ C_3[\sin(\beta_n x) + \sinh(\beta_n x)] + C_4[\sin(\beta_n x) - \sinh(\beta_n x)] \quad (22)$$

It is important to introduce the boundary conditions for a cantilever condition, which are that the fixed end of the cantilever has a zero displacement and zero slope, while the free end has no bending moment or shear force. These aforementioned conditions can be represented as shown in Equations 20 (fixed end) and 21 (free end). The general solution of (18) can be represented by a linear combination of Equations specified in (22), using a zero displacement boundary condition in it we get $C_1=0$. The first derivative of Equation 22, applying zero sloped boundary condition to it we obtain $C_3=0$.

$$\frac{\partial X(x)}{\partial x} = C_2[-\sin(\beta_n x) - \sinh(\beta_n x)] + C_3[\cos(\beta_n x) + \cosh(\beta_n x)] + C_4[\cos(\beta_n x) - \cosh(\beta_n x)] \quad (23)$$

For the bending moment (second derivate) and shear force (third derivate), we get the following set of conditions given below. Combing (24) and (25) we get the following relation between C_2 and C_4 which can be substituted into Equation 22 to give us the equation for mode shapes of a cantilever beam (Equation 27).

$$\frac{\partial^2 X(x)}{\partial x^2} = C_2[-\cos(\beta_n L) - \cosh(\beta_n L)] + C_4[-\sin(\beta_n L) - \sinh(\beta_n L)] = 0 \quad (24)$$

$$\frac{\partial^3 X(x)}{\partial x^3} = C_2[\sin(\beta_n L) - \sinh(\beta_n L)] + C_4[-\cos(\beta_n L) - \cosh(\beta_n L)] = 0 \quad (25)$$

$$C_4 = C_2 \frac{\sin(\beta_n L) + \sinh(\beta_n L)}{-\cos(\beta_n L) - \cosh(\beta_n L)} \quad (26)$$

$$X_n(x) = C_2 [[(\cos(\beta_n x) - \cosh(\beta_n x)) \cdot (-\cos(\beta_n L) - \cosh(\beta_n L))] \\ (\sin(\beta_n x) - \sinh(\beta_n x)) \cdot (\sin(\beta_n L) + \sinh(\beta_n L))] \quad (27)$$

The constant C_2 is generally found by integrating the square of the mode shape Equation 27 between the limits 0 and L. The frequency equation for a cantilever beam can be found by plugging in Equation 26 into either Equation 24 or 25,

$$\cos(\beta_n L) \cosh(\beta_n L) = -1 \quad (28)$$

The above equation is the characteristic equation of a cantilever beam whose natural frequency can be found by using the roots of the Equation 28 and substituting it in Equation 29. A few roots as shown in Table 2.1. Using Equation 27 the first four mode shapes of a cantilever energy harvester beam were plotted and is shown in Figure 2.1.

$$\omega_n = \frac{(\beta_n L)}{L^2} \sqrt{\frac{EI}{\rho A}} \quad (29)$$

Table 2.1

Roots for the characteristic equation of a cantilever beam

N	$\beta_n L$
1	1.87510
2	4.69409
3	7.85475

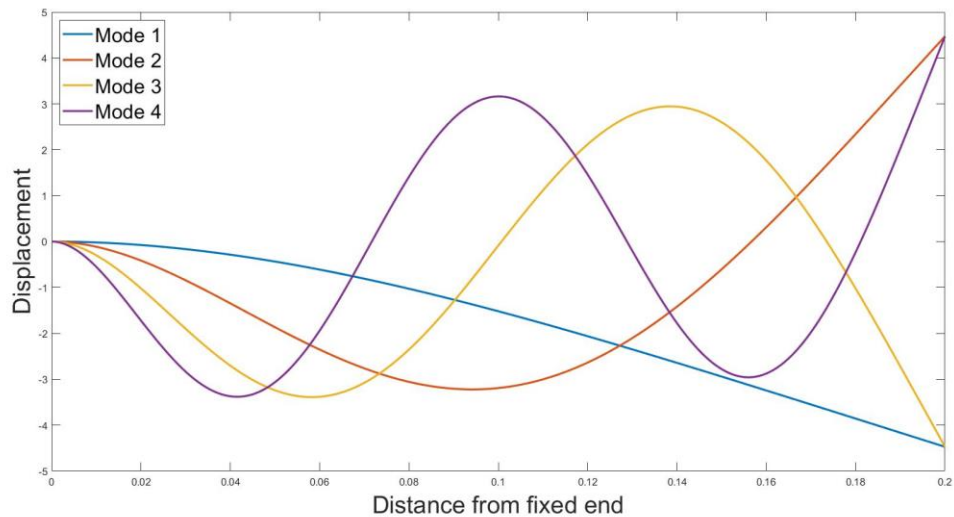


Figure 2.1 First four modes of the energy harvester cantilever beam

2.2. Second Assumption

The second assumption made in deriving the coupled electromechanical governing equation of motion is the application of the Euler-Bernoulli beam theory. Following the theory, strain in the beam can be written as a product of the second derivative of the displacement with respect to the position along the beam and distance from the neutral axis. After defining the strain with this theory strain S can be written as,

$$S = -y \frac{\partial^2 u(u,t)}{\partial x^2} = -y \phi(x)'' r(t) \quad (30)$$

2.3. Third Assumption

The last assumption made is that there is a constant electric potential across the piezoelectric patch and no potential is applied to the beam. In mathematical form it can be written as follows:

$$E = \psi(x) \text{vol}(t) = \begin{cases} \frac{-\text{vol}}{t_p} & \frac{t}{2} < y < \frac{t}{2} + t_p \\ 0 & -\frac{t}{2} < y < \frac{t}{2} \end{cases} \quad (31)$$

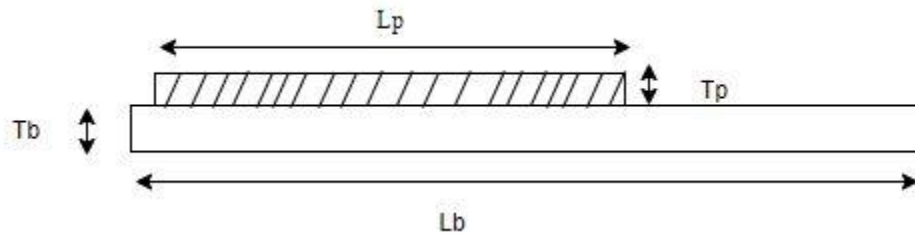


Figure 2.2 Energy harvester beam schematic

This assumption is an application of a unimorph configuration with the patch being placed on the top side of the beam. In Equation 31 t_p is the thickness of the patch and t_b is the thickness of the beam. A representation of this is shown in Figure 2.2.

2.4. Compact Equation for Energy Harvester Model

Based on the assumptions defined in Sections 2.1, 2.2 and 2.3, Equation 13 can be simplified to represent the physical parameters of a unimorph piezoelectric Euler-Bernoulli beam. This makes the modeling not only easier but also the equation becomes similar to most other equations of motions used for modeling energy harvesters (Liao & Sodano, 2008; Sodano et al., 2004; Song et al., 2007)

The parameters described below include the mass matrix (M), stiffness matrices (K), and electromechanical coupling term (Θ) and, capacitance matrix (C_p).

$$M_B = \int_0^{L_B} w_B \rho_B \phi^T(x) \phi(x) t_B dL_B \quad (32)$$

$$M_P = \int_{L_{P1}}^{L_{P2}} \int_{\frac{t_B}{2}}^{\frac{t_B}{2} + t_P} y w_P \rho_P \phi^T(x) \phi(x) dy dL_P \quad (33)$$

$$K_B = \int_0^{L_B} \int_{\frac{t_B}{2}}^{\frac{t_B}{2}} y^2 w_B \phi^T(x) c_B \phi(x) dy dL_B \quad (34)$$

$$K_P = \int_{L_{P1}}^{L_{P2}} \int_{\frac{t_B}{2}}^{\frac{t_B}{2} + t_P} y^2 w_P \phi^T(x) c_P \phi(x) dy dL_P \quad (35)$$

$$\Theta = \int_{L_{P1}}^{L_{P2}} \int_{\frac{t_B}{2}}^{\frac{t_B}{2} + t_P} -y w_P \rho_P \phi^T(x) c_B d_{31} \frac{1}{t_P} dy dL_P \quad (36)$$

$$C_P = \frac{K_{33} \epsilon_o w_P (L_{P2} - L_{P1})}{t_P} \quad (37)$$

$$\begin{aligned} V.I = \int_{t_1}^{t_2} & \left[\delta r^T(t) (M_B + M_P) \dot{r}(t) - \delta r^T(t) (K_B + K_P) r(t) \right. \\ & + \delta r^T(t) \theta \text{vol}(t) + \delta \text{vol}(t) \Theta^T r(t) + \delta \text{vol}(t) C_P \text{vol}(t) \\ & \left. + \sum_{i=1}^{nf} \delta r(t) \phi(x_i)^T f_i(t) - \sum_{j=1}^{nq} \delta \text{vol} q_j(t) \right] dt = 0 \end{aligned} \quad (38)$$

In Equations 32 - 37 L_B is the length of the beam, L_P is the length of the patch, y is the thickness function, c_B and c_P are Young's modulus of the beam and patch respectively, d_{31} is the piezoelectric coefficient, K_{33} is the dielectric constant and ϵ_o is the absolute permittivity whose value is $8.854e-12$. To obtain the equation of motion of the

coupled electromechanical system, we combine the Equations described in 32 – 37 with 14, 30 and 31 we get (38).

In Equation 38, $\delta()$ indicated the variation of the corresponding variables. The integral of V.I makes way for two coupled equations, related by the term Θ . The two equations defined the mechanical and electrical properties of the system respectively.

$$\begin{aligned} (M_B + M_p) \ddot{r}(t) + (K_B + K_p)r(t) - \Theta \text{vol}(t) &= \sum_{i=1}^{nf} \phi(x_i)^T f_i(t) \\ \Theta^T r(t) + C_p \text{vol}(t) &= q(t) \end{aligned} \quad (39)$$

The above equations are the equation of motion of a coupled electromechanical system with a piezoelectric material and described the motion of the energy harvester beam. In Equation 39 no term that accounts for the energy dissipated by the systems but in the real world scenario, there will be some amount of energy lost by the system. This discrepancy can be accounted for by using Ohm's law by the addition of a resistor to the system. The resistor does provide a way for representing energy lost from such a system which can be expressed mathematically as (40),

$$\text{vol}_i(t) = -R \dot{q}(t) \quad (40)$$

This only represents the electrical energy loss term. To obtain a better model addition of a mechanical damping term is also extremely important, which will give us a better power prediction. The damping term is usually found from experiments such as Frequency Response Functions (FRFs) or by using logarithmic decrement. The damping ratio ζ found from the previously described methods can then either be used directly or used to find the damping matrix C.

After accounting for both the electrical and mechanical damping terms, the coupled electromechanical governing Equation 39 becomes:

$$\begin{aligned}
M \ddot{r}(t) + K r(t) + C \dot{r} - \Theta \text{vol}(t) &= F(t) \\
\Theta \dot{r} + C_p \text{vol}(t) + \frac{V}{R} &= 0
\end{aligned}
\tag{41}$$

Where,

$$\begin{aligned}
M &= M_B + M_P \\
K &= K_B + K_P
\end{aligned}
\tag{42}$$

The only term left to be defined in the equation of motion is the force term $F(t)$.

Based on the previous research papers, all the experiments performed on such systems the beam were subject to base excitations on the clamped end of the structure. The force subjected at the clamped end is in-turn transferred to the beam. The forcing function $F(t)$ is defined in (43), where ω_f is the forcing frequency, which is the frequency at which the experiment or simulation is performed and A_0 is the amplitude of base displacement.

$$\begin{aligned}
F(t) &= \int_0^{L_B} \phi(x) \rho_B \omega_f^2 A_0 w_B t_B \\
&\quad \int_{L_{P1}}^{L_{P2}} \phi(x) \rho_P \omega_f^2 A_0 w_P t_P
\end{aligned}
\tag{43}$$

2.5. Implementation of a Varying Cross-Section of the Energy Harvester Model

To implement a varying width, the previously derived model needs to be changed. As seen from Equations 32 – 37 mode shapes are an integral part of most of the terms if not all and by using a varying width profile this would imply that the same mode shape equations cannot be used as that used for a constant width case. An exponentially varying width will be used in this thesis, therefore the correct mode shape equations need to be used for that case. Where W_{B0} is the width of the beam at the clamped end and x is the position along the x -axis.

$$W_B = W_{B_0} e^{(\delta x)} \quad (44)$$

The mode shape equation described by Ece et al. (2006) for a varying width case will be used in this thesis. The results from Ece et al was validated against multiple researches (Cranch & Adler, 1956; Tong et al., 1995) for cases of three types of beam configurations which are simply supported, clamped-clamped and clamped-free. Since the model was derived for a cantilever beam configuration, the clamped-free case will be used. The mode shape equation for a cantilever beam with a varying width is shown below,

$$\phi(x) = e^{-\frac{\delta}{2}x} [b_1 \cos(\lambda_1 x) + \sin(\lambda_1 x) - b_1 \cosh(\lambda_2 x) + b_4 \sinh(\lambda_2 x)] \quad (45)$$

Where b_1 , b_4 , λ_1 and λ_2 are defined as,

$$b_1 = \frac{2\lambda_1(2\delta\lambda_2 - \delta^2 - 2\omega)e^{2\lambda_2} - 4\lambda_2[2\delta\lambda_2 \cos\lambda_1 + (2\omega - \delta^2)\sin\lambda_1]e^{\lambda_2} + \lambda_1(2\lambda_2 + \delta)^2}{\lambda_2 \{2(2\delta\lambda_2 - \delta^2 - 2\omega)e^{2\lambda_2} + 4[(\delta^2 - 2\omega)\cos\lambda_1 + 2\delta\lambda_1 \sin\lambda_1]e^{\lambda_2} - (2\lambda_2 + \delta^2)\}} \quad (46)$$

$$b_2 = -\frac{\lambda_1}{\lambda_2} \quad (47)$$

$$\lambda_1 = \frac{\sqrt{4\omega - \delta^2}}{2} \quad (48)$$

$$\lambda_2 = \frac{\sqrt{4\omega + \delta^2}}{2} \quad (49)$$

In Equations 45 – 49 ω is the natural frequency and δ is the width-varying parameter which can be any number. The first mode shape for $\delta = -0.5, 0, 0.5$ was plotted for a non-dimensionalized cantilever beam and is shown in Figure 2.5, which is the same as the one described in Ece et al. (2006). A negative value of δ signifies an exponentially decreasing width while a positive value of δ is for an exponentially increasing width. δ equal to zero,

represents a constant width beam. Figure 2.3 shows the effect of delta of the width, for positive value of δ the width increase (left) and for negative value of δ width negative (right).

The plot shown in Figure 2.5 is for a normalized beam and the same plot was obtained by Ece et al. (2006), therefore it can be concluded that the mode shape equations are in accordance with one published in the paper described before. These mode shape equations were then used in the mathematical model and the width ' W_B ' was then replaced by (44) in Equations 32 – 37 and 43. In order to verify if the mode shape equations were correctly implemented, the model was run for delta (δ) equal to zero. For this value of delta, the same voltage should be obtained as that for a constant width beam. After the code was run in Matlab the same voltage value was obtained and hence it was concluded that the implementation of a varying width beam was performed correctly.

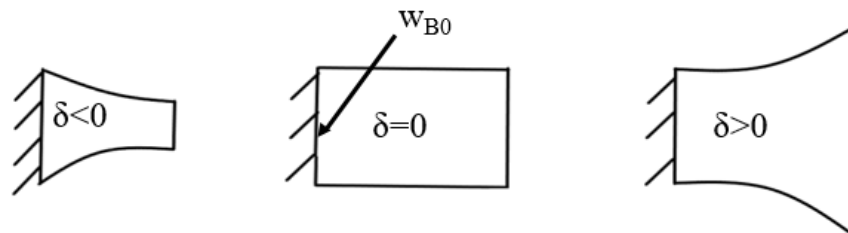


Figure 2.3 Variation of width with delta (δ)

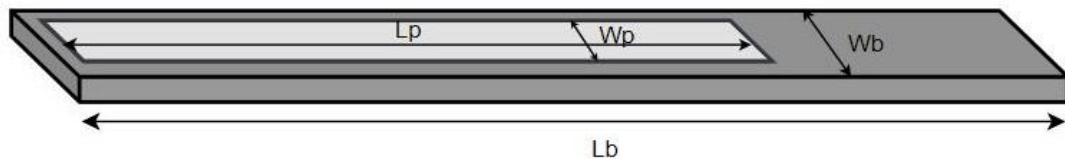


Figure 2.4 Different parameters of the energy harvester beam

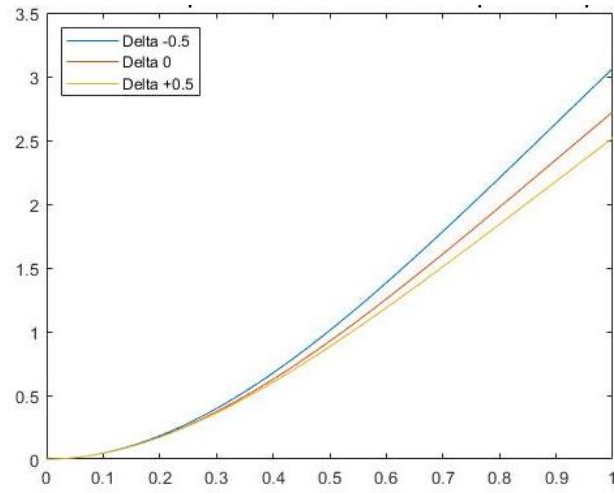


Figure 2.5 Mode shapes for cantilever beam for different values of delta (δ)

3. Model Validation

In this chapter, we will discuss the validation of the mathematical model of an MFC based energy harvester developed based on the governing equations of the motion derived in Chapter 2. The different inputs required to obtain the output voltage in the mathematical model developed in Matlab will be stated. This model was validated with experiments performed using an energy harvester beam purchased from Smart Materials Corp. Frequency response functions (FRF) of energy harvester beam were obtained by performing forced vibrations experiments on the beam, to compare the natural frequency obtained from the model versus the experimental frequencies. Results from both experiments will be discussed and possible reasons for discrepancies will also be stated.

3.1. System Identification Experiment

The identification of the first natural frequency of this energy harvester beam is extremely important since this will determine the frequency range for which the experiment will be performed. For this system identification frequency response functions will be generated using a shaker type of experiment.

Any linear-time variant (LTI) system can be described by a constant linear ordinary differential equation (ODE). In Equation 50 the right-hand side of the equation has the input (excitation) $x(t)$ and the output (response) $y(t)$ is on the left-hand side along with its derivatives. To solve for $y(t)$, the ODE needs to be solved for every different $x(t)$. This is done by assuming a complex exponential for the input shown in Equation 51 and output shown in Equation 52, where X and Y are the phasor representations of the input and output respectively. Substituting these in the ODE we get (53). The ratio between the

output phasor Y and input phasor X is defined as the frequency response function (FRF) $H(j\omega)$ shown in Equation 53.

$$\sum_{i=0}^n a_i \frac{d^i}{dt^i} y(t) = x(t) \quad (50)$$

$$x(t) = X e^{j\omega t} \quad (51)$$

$$y(t) = Y e^{j\omega t} \quad (52)$$

$$Y = H(j\omega)X \quad \text{or} \quad H(j\omega) = \frac{Y(t)}{X(t)} \quad (53)$$

There are two main ways to obtain these frequency response functions: an impact hammer test and a vibration test (using a shaker). Conceptually both the test are similar but the principle excitation method is different for these types of tests. In both these types of tests, there are two types of transducers used, one to measure the input (force transducer) and the other to measure the response or output of the system (accelerometer) in response to the given input. Both these transducers are passed through a signal conditioner to either an FFT analyzer or can be recorded by using data acquisition systems in conjunction with a software such as LabVIEW.

The difference between the two methods is that in the shaker type of experiment shown in Figure 3.1 a shaker along with a signal generator and power amplifier is used while in an impact hammer method as the name suggests an impact hammer is used as shown in Figure 3.2. All the modes are excited for an impact hammer type of test, while in the shaker method only the modes that fall within the frequency ranger of the signal generated will be excited.

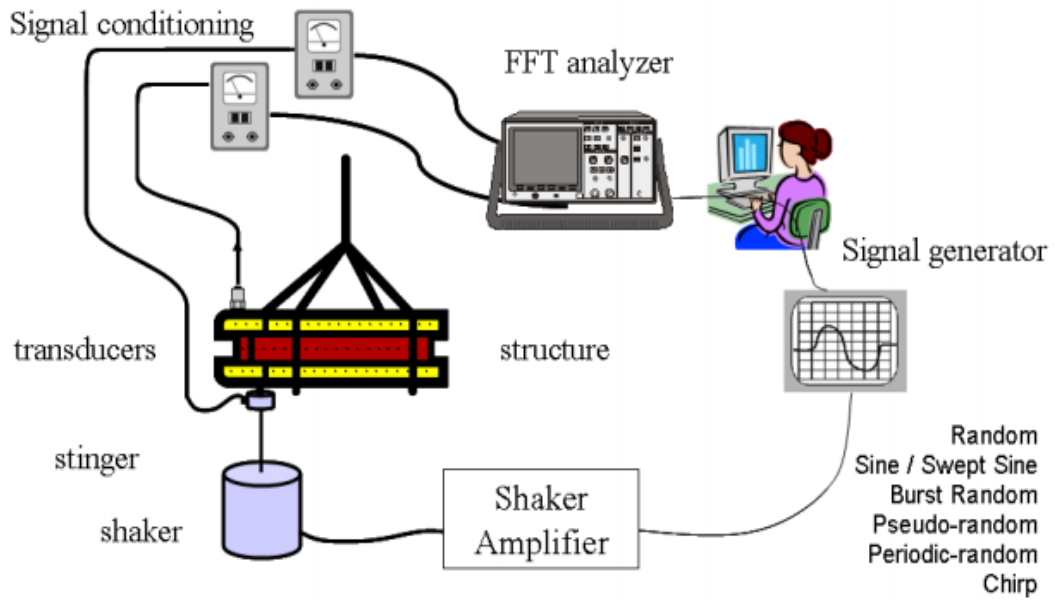


Figure 3.1 Vibration test using shaker (Modal Shop Inc)

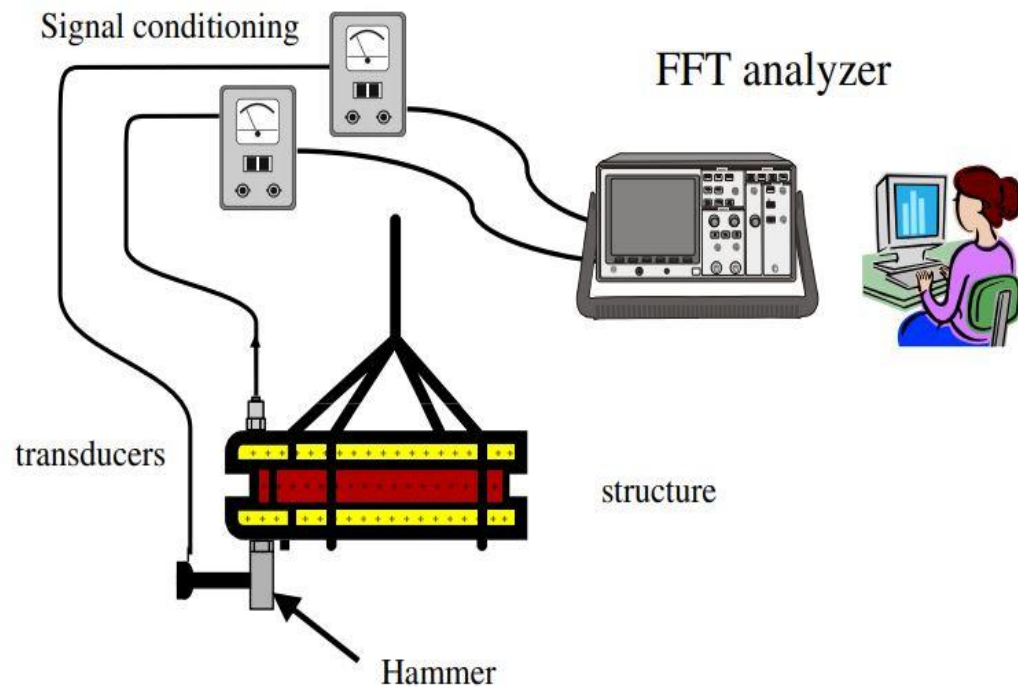


Figure 3.2 Impact hammer test (Modal Shop Inc)

In this research, the shaker method was chosen to obtain the frequency response functions. For the function generation a Tektronix AFG 3051C along with Brüel and Kjær type 2718 power amplifier is used as shown in Figure 3.3. The power amplifier was connected to a type 4810 Brüel and Kjær mini shaker on which the energy harvester glass fiber beam was attached with an MFC M8528P2 patch which was obtained from Smart Material Corp. A Brüel and Kjær type 8230 force transducer was attached between the shaker and the beam. On the beam, two accelerometers from PCB Piezotronics were attached as shown in Figure 3.4.

The force transducer and accelerometers were attached to the National Instruments 9147 data acquisition (DAQ) system through a PCB Piezotronics model 482C signal conditioner shown in Figure 3.5. The DAQ system was attached to PC and all the data was recorded using LabVIEW. The data recorded from the force transducer served as the input to the system while the accelerometers served as the response or output of the system. The accelerometers were capable of recording acceleration of $\pm 490 \text{ m/s}^2$ within a range of 1-8000 Hz and has a sensitivity of $10.2 \text{ mV/ (m/s}^2)$. The force transducer was capable of recording $\pm 45 \text{ N}$ within a range of 0.01-36000 Hz and had a sensitivity of 105.3 mV/N .

To conduct the experiment a sine sweep from 1-100 Hz was supplied to the shaker via the signal generator and power amplifier. The sine sweep was set for 120 seconds. As shown in Figure 3.4 two accelerometers were used for every experiment run. The locations of the accelerometers were varied from the base of the cantilever up to almost half the length of the beam. Data was recorded for each set of locations and the same frequency range for the sine waves and the same duration was set as stated earlier.

Although the accelerometers were light in weight they still added to the mass of the beam. Attaching the accelerometers closer to the tip may have altered the first mode frequency more due to the added mass of the accelerometers, hence the accelerometers were not taken beyond half the length of the beam.



Figure 3.3 Tektronix function generator (AFG 3051C) and Brüel and Kjær power amplifier (Type 2718)

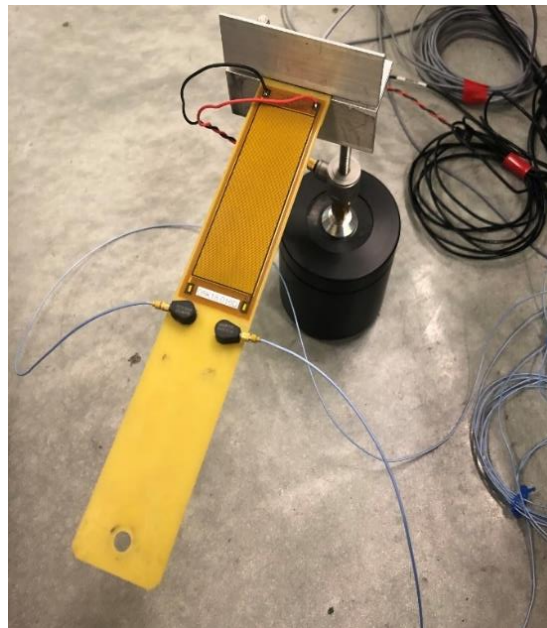


Figure 3.4 Glass fiber beam with MFC (M8528P2) patch and PCB accelerometers

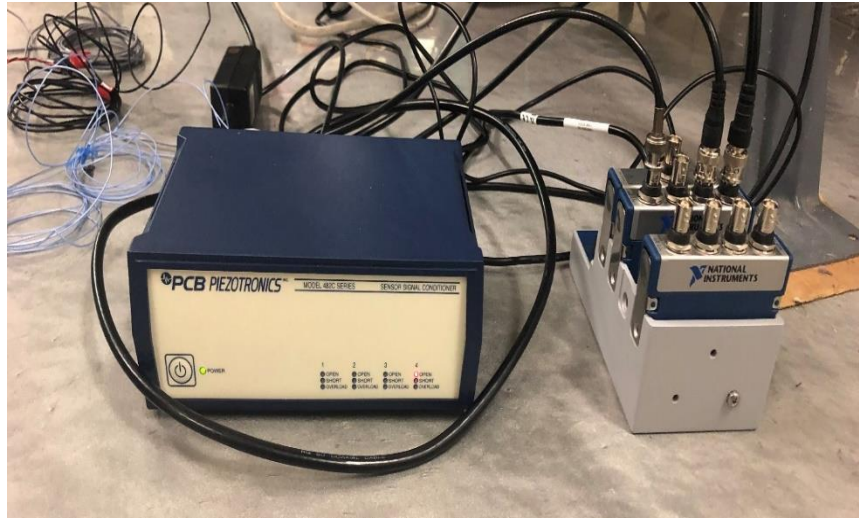


Figure 3.5 PCB signal conditioner (Model 482C) and National Instruments DAQ (NI 9174)

The data from both the sensors were sampled at a rate of 2048 Hz. The accelerometers were placed at six different locations and a total of twelve data sets were recorded from the accelerometers and six from the force transducers. A sample of the data recorded from the two accelerometers and force transducer from one location is shown in Figure 3.6.

After recording all data using LabVIEW, the data was then processed on Matlab. The first process was to convert the data from the time domain to the frequency domain. Then using the pre-defined bode plot function in Matlab, frequency response functions were generated. In Figure 3.7 a frequency response function of one set recorded data is shown, it is seen that the first bending mode frequency from the plot is 27.5 Hz. Since multiple data sets were recorded for different locations of the accelerometer it was necessary to see which results gave the accurate first natural frequency. For this, a state-space model was generated in Matlab using `n4sid` pre-defined function which generates an estimated state-space model from time-domain or frequency domain data.

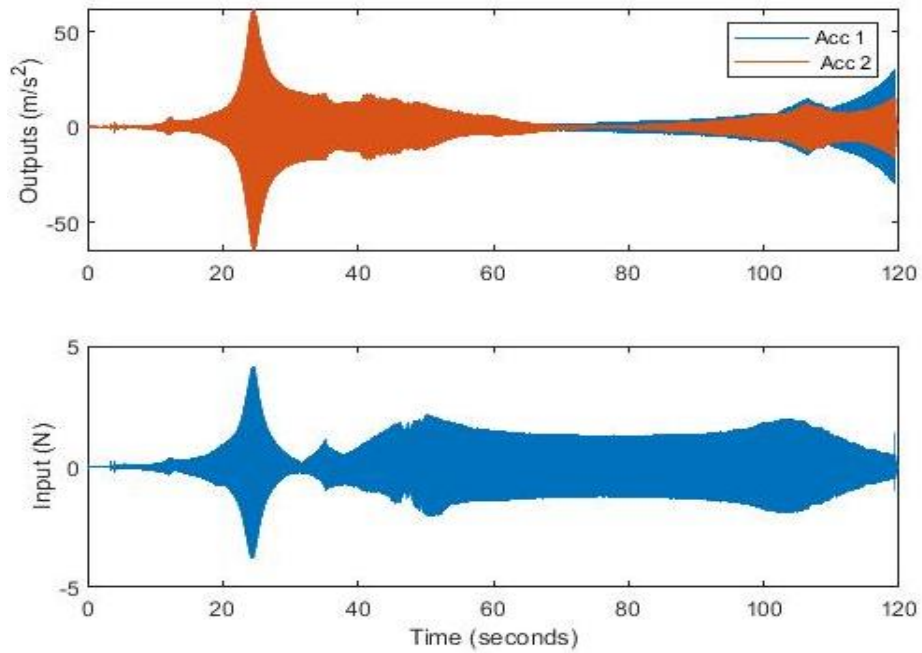


Figure 3.6 Sample input and output recorded from the transducers

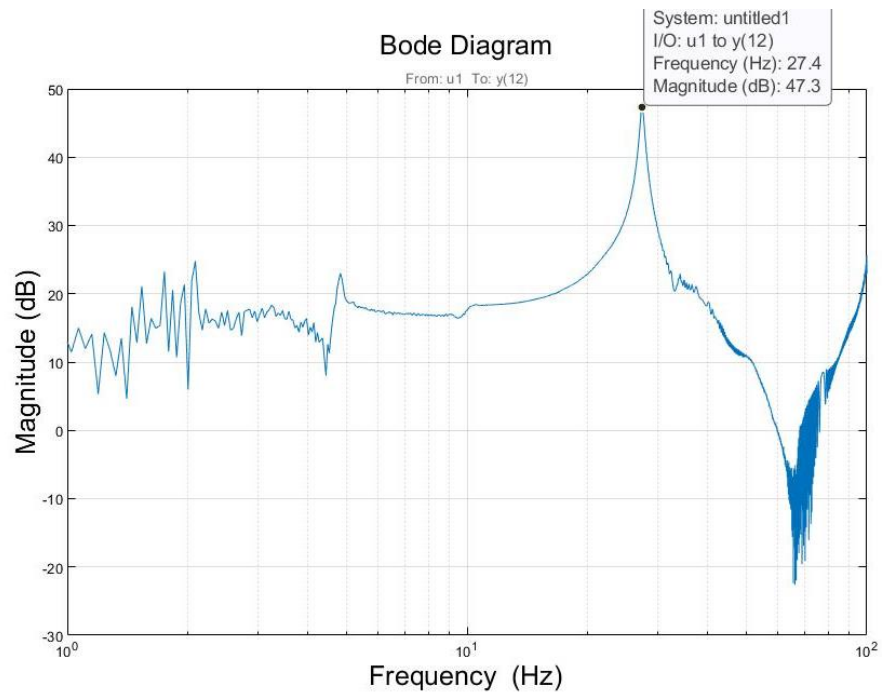


Figure 3.7 Frequency response functions generated using bodeplot for one set of recorded data

This process was performed for all the recorded data sets. Then a comparison was made for each data set and its corresponding state-space model, bode plots were generated from which the best and worst fits generated are shown in Figure 3.8. In Figure 3.8 the top figure shows the worst fit and the below figure shows the best first obtained. A normalized root-mean-square-error method was used to obtain these fits. The red line shows the generated model and the blue line shows the bode plot generated from the recorded data. It can be seen that the best fit occurs for the 12th set of data recorded which gives us a first natural frequency of 27.5 Hz. Therefore it was concluded that the first natural frequency from the FRF experiments was 27.5 Hz.

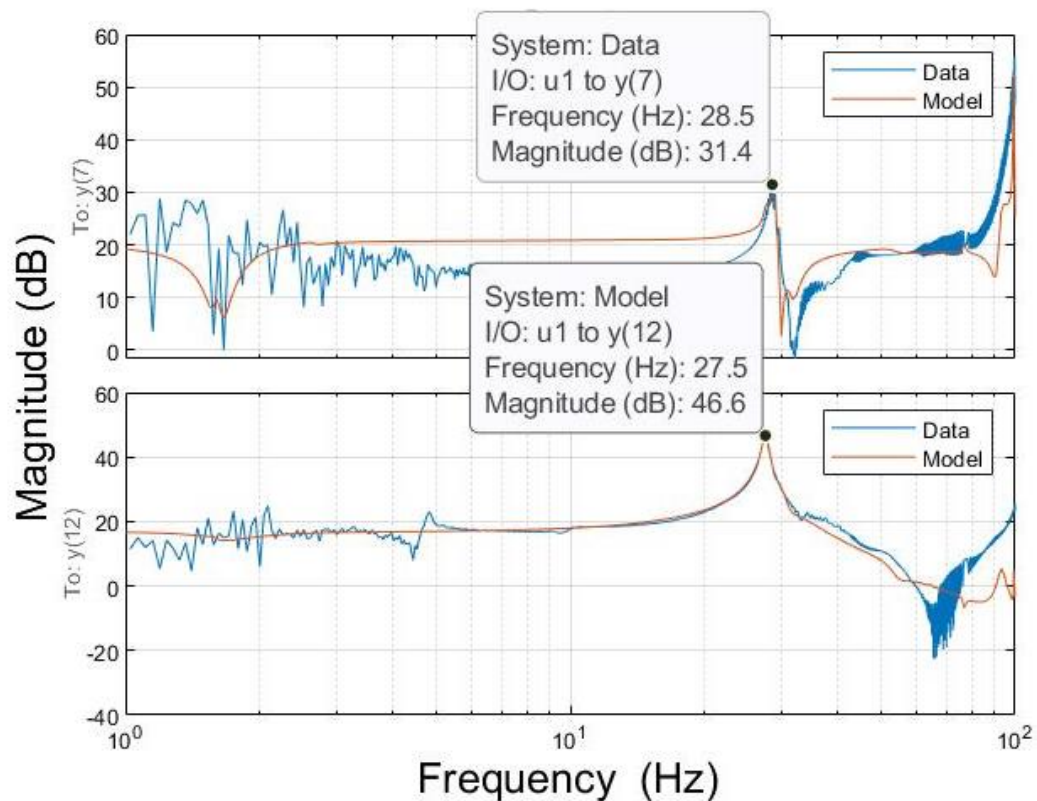


Figure 3.8 Worst (top) and best (bottom) fits between the state space and experimental data

3.2. Energy Harvester Experiments

From the FRF experiments, it was found that the first natural frequency of the energy harvester beam was approximately 27.5 Hz, hence it could be that the range of the experiment should include at least ± 5 Hz frequencies around this to account for the error. To set up the experiment for the energy harvesters, references from previous stated researches (Liao & Sodano, 2008; Sodano et al., 2004; Song et al., 2007) were used to keep the experimental setup as similar to these as works possible since the model developed in this thesis was based upon the equations used in these papers. Hence the model validation was also done with a similar experimental setup is used.

An experimental flow with all the necessary equipment's required to conduct the experiment is shown in Figure 3.10. Using a signal generator along with a power amplifier a constant frequency sine wave is supplied to the shaker. The beam which is mounted on the shaker is subject to this base excitation. The voltage across the MFC patch is read on the oscilloscope. As mentioned in Chapter 2 an electrical resistance needs to be provided to account for the loss of energy which is provided before the voltage is read on the oscilloscope. On the base of the clamping cantilever structure, an accelerometer is used.

The readings from the accelerometer were read on a PC via a data acquisition system. Also, a signal conditioner is used in conjunction with the accelerometer and the data acquisition system. The accelerometer is used to measure the excitation force applied by the shaker. Another alternative is to use a load cell, connected on the shaker sting, for measuring the excitation force. It is made sure that the same value of excitation force is applied by the shaker at all the vibration frequencies. The formula used to calculate the

amplitude of base excitation is shown in Equation 54, where a is the magnitude of base acceleration which is kept the same for all frequency levels, A_{\max} is the maximum amplitude of displacement and ω is the excitation frequency. A_{\max} substituted for A_0 in Equation 43.

$$A_{\max} = \frac{a}{\omega^2} \quad (54)$$

The same signal generator and power amplifier were used as shown in Figure 3.3. Although the same shaker and beam were used the setup was slightly different than the one used in Figure 3.4. For the energy harvester experiment, the setup for the beam and shaker with the accelerometer is shown in Figure 3.11. It can be seen that the accelerometer is kept on the clamping. The resistance module used in this setup is shown in Figure 3.9 and was included in the energy harvesting kit purchased from Smart Material Corp's. In the resistance module, each division was supposed to be multiplied with $50K\Omega$ to obtain the correct resistance values and this was verified with a multimeter. Properties of the MFC patch used are stated in Table 3.1 and a list of the properties of the glass fiber composite beam are given in Table 3.2 which was given by Smart Material Corp.

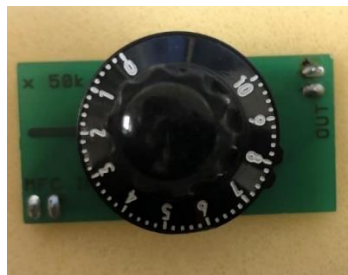


Figure 3.9 Variable resistance module from Smart Material Corp

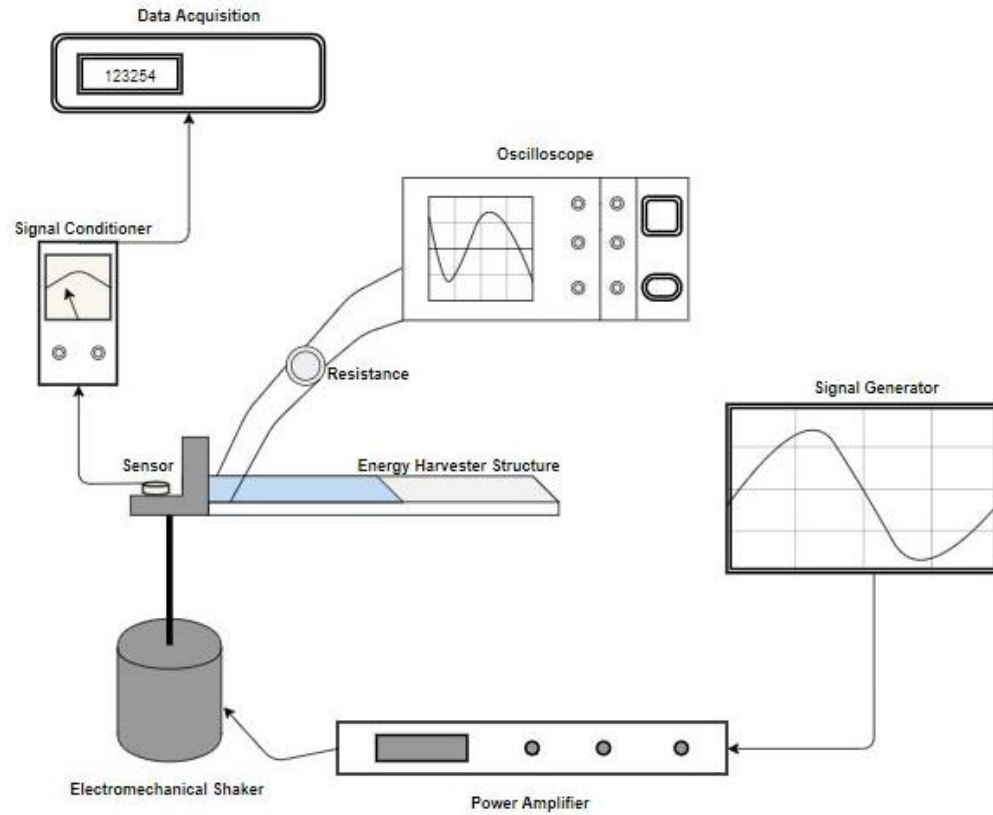


Figure 3.10 Experimental flow diagram



Figure 3.11 Beam setup for energy harvester experiment with accelerometer at base

Table 3.1

List of properties of the MFC patch

Properties	Symbol	Value
Dielectric constant	K_3^T	1800
Piezoelectric coefficient	d_{31}	-2.1e-10(m/volt)
Density of patch	ρ_P	5440 (kg/m ³)
Young's modulus	E_{PZT}	30.336 GPa
Length of patch	L_P	108 mm
Thickness of patch	t_P	0.3 mm
Width of patch	w_P	31 mm

Table 3.2

List of properties of the glass fiber composite beam

Properties	Symbol	Value
Density of beam	ρ_B	2540 (kg/m ³)
Young's modulus	E_{beam}	70.5 GPa
Length of beam	L_B	200 mm
Thickness of beam	t_B	1.10 mm
Width of beam	w_B	34 mm

3.3. Inputs for Matlab Model

Before the results from the experiment are compared with the energy harvester Matlab model, the different inputs required to obtain the voltage from the model are discussed. In this research, the model that will be used will be a single-mode model. The reason for using just the first mode is that the maximum voltage is generated at the maximum strain which occurs at the first bending mode. It is assumed that the beam goes through only bending modes and no torsional modes. Another important reason for developing a single-mode model can be attributed to the fact that the optimization

becomes much easier and less computationally costly since a state-space model doesn't need to be generated which would be needed if a multiple mode model was developed.

To obtain the voltage, the different inputs needed as shown in Figure 3.12. This relation of the inputs is obtained from equation 41 which was derived in Chapter 2, which is the governing equation for any coupled electromechanical system containing a piezoelectric material. Therefore in order to find the unknown in Equation 41 (which is the voltage in this case), the terms required are the mass matrix, stiffness matrix, damping ratio, electromechanical coupling term, piezoelectric capacitance term, resistance, and the excitation force. The boxes shown in red are obtained from materials properties, dimensions properties, and modes shapes. How each of those terms in the red boxes are obtained is shown in Figure 3.13. The derivation of each term was discussed in Chapter 2 and are defined in Equations 32 – 37. It can be seen the mode shapes are an integral part for the calculation of different properties. Hence, during the shape optimization process of the beam (discussed in Chapter 4), any change in shape requires an update to the mode shapes.

The terms shown in white i.e. resistance, damping ratio, and force are obtained from either an experiment or just an input to the system which can be set to any desired value. A depiction of this is shown in Figure 3.14. Force term is the one that is obtained from the energy harvester experiment at the frequency at which the experiment is conducted and amplitude of base acceleration as calculated in (54). This amplitude of the base acceleration term is substituted as A_0 in Equation 43.

The damping ration ζ was obtained from two main experiments the FRF and logarithmic decrement. From the FRF the value of ζ was 0.02 while the value of ζ

obtained from multiple trials of logarithmic decrement ranged from 0.01 – 0.05. For the Matlab model, a value of 0.03 was used since it was close enough to the one obtained from the FRF and also is the mid-point of the range obtained from the logarithmic decrement. Also using this value of ζ decreases the error between the voltage obtained from the model and that obtained from the experiment.

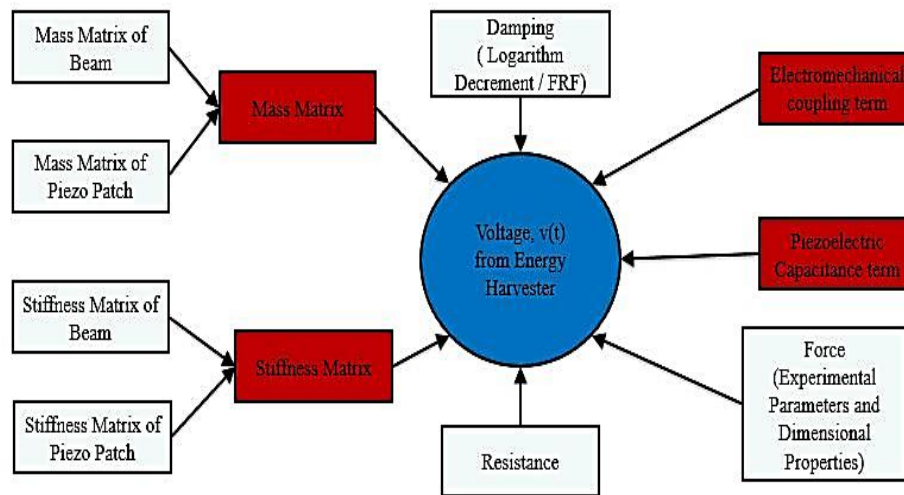


Figure 3.12 Different inputs needed for voltage from Matlab model

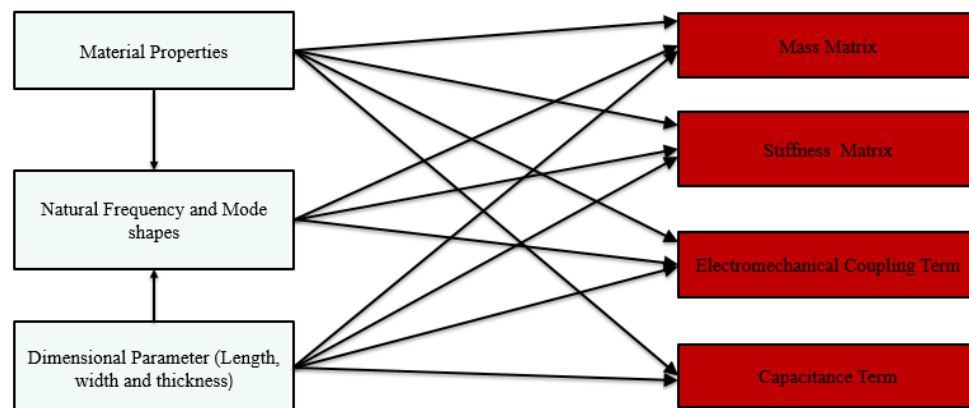


Figure 3.13 Inputs for mass, stiffness, electromechanical coupling matrices and capacitance term

Lastly, the Equation 55 will be used for voltage calculation. This is the same equation used by Song et al. (2007) that they have validated with experiments. The same equation for voltage will be used for the optimization.

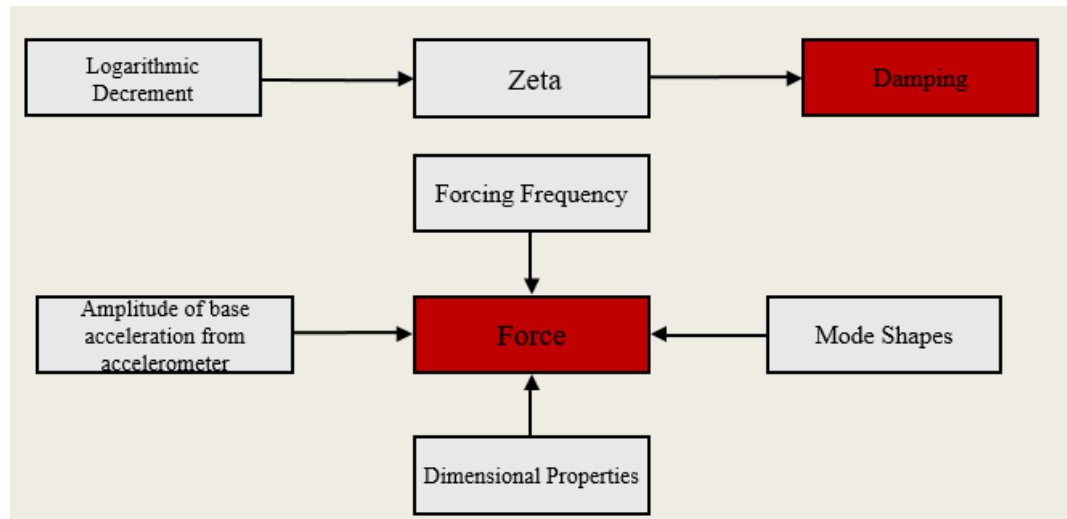


Figure 3.14 Terms obtained from experiment

$$v = \left(\frac{\Theta R F}{\sqrt{2} M} \right) \frac{1}{\sqrt{\left[\left(\frac{\Theta^2 R}{M} + C_p R (\omega_n^2 - \omega^2) + 2\zeta \omega_n \right)^2 + \left(\frac{\omega_n^2}{\omega} - \omega - 2\zeta \omega \omega_n C_p R \right)^2 \right]}} \quad (55)$$

In Equation 55 ω_n is the natural frequency of the beam and is obtained as shown in Equation 56. Alternatively, Equation 29 can also be used for the calculation of the natural frequency. In this thesis Equation 56 was preferred since the natural frequency obtained from it was 27.8 Hz which was extremely close to the natural frequency obtained from the FRF experiments. Another reason is also that the same expression for natural frequency was used by multiple researches (Liao & Sodano, 2008; Song et al., 2007) in which both developed a single-mode model.

$$\omega_n = \sqrt{\frac{K}{M}} \quad (56)$$

3.4. Results and Discussion

The experiment and model were set up to run for the same set of inputs and the frequency range 21-31 Hz. A comparison of the voltage obtained from the experiment and the model is shown in Figure 3.15 and Table 3.3. The base acceleration was kept constant at $\pm 2.5 \text{ m/s}^2$ for all the frequencies and the value of resistance was $102 \text{ K}\Omega$.

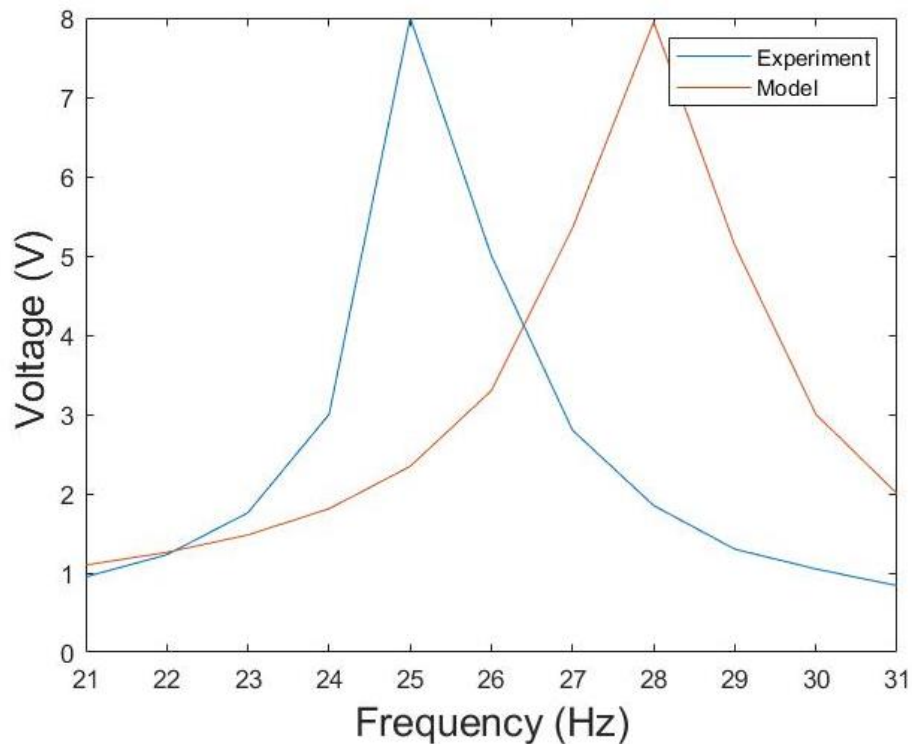


Figure 3.15 Voltage output from Matlab model and experiment

As seen in Figure 3.15 there is some discrepancy in the results between the model and the experiments. In the experiment, the maximum voltage output is at the frequency of 25 Hz, while in the model the maximum voltage is at 28 Hz. Since the maximum voltage is

always obtained at the first natural frequency according to the model it is at 28 Hz while for the experiment it is 25 Hz. Another discrepancy is that in the model the voltage obtained in the frequencies ranges below 25 Hz the voltage has an error of around 30%-40% when compared to that obtained from the experiment.

Table 3.3

Voltage obtained from mathematical model and experiment at different frequencies

Frequency(Hz)	Voltage (V) – Model	Voltage (V) – Experiment
21	1.10	0.95
22	1.26	1.23
23	1.48	1.76
24	1.81	3
25	2.345	8
26	3.3	5
27	5.35	2.8
28	7.95	1.85
29	5.13	1.30
30	3.0	1.05
31	2	0.84

The reason for these discrepancies can be attributed to a few things, (a) the value of base amplitude A_{\max} that is calculated from the values of base acceleration, as explained in section 3.3, is only an approximation of the correct force input to the numerical model of the energy harvester, (b) the model only accommodates the first mode whereas other modes do contribute in a small extent to the response close to the first mode frequency, (c) the damping ratio used in the model is only an approximate and chosen from a range of values as discussed in the previous section of this chapter, and (d) the value of resistance used maybe not be the optimal one therefore using an optimal value could give better results.

An important discussion to be made for the difference in the frequency at which the voltage peak is observed in the experiment versus model is the resistance at which the experiment is performed. There have been multiple studies performed on using an optimal value of resistance to perform the experiment and also how it could shift the frequency at which the peak value of voltage is obtained. The resistance used in the experiment may be interpreted as an electrical damping term. Hence a change in the resistance results in a change in the voltage harvested by the beam. It also affects the dynamic characteristics of the system such as the frequency at which peak voltage is obtained, and the peak displacement or stress in the beam. In the study performed by Liao and Sodano (2008) they investigated how the value of resistance at which the experiment is performed changes the results. As can be seen in Figure 3.16, at different values of resistance the peak value of voltage varied with the frequency.

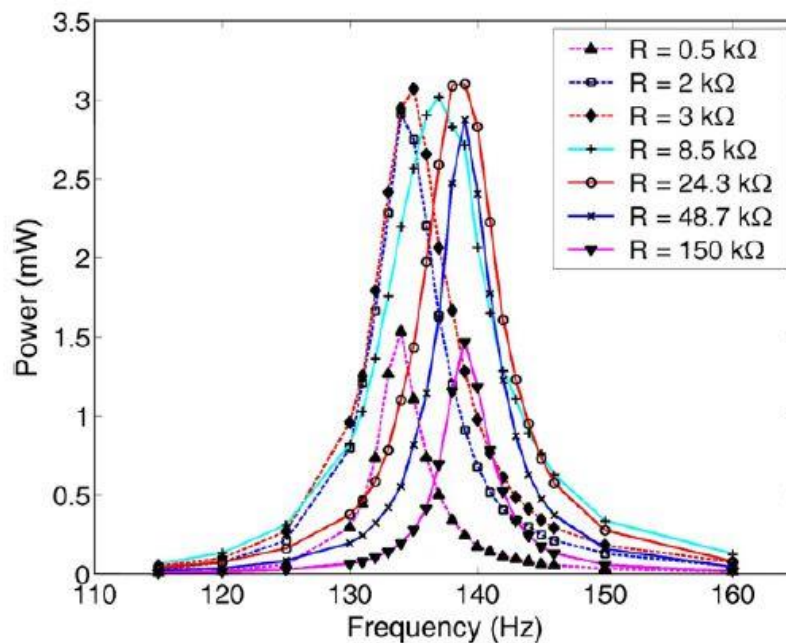


Figure 3.16 Variation of frequency at which peak power is obtained at different values of resistance (Liao & Sodano, 2008)

In another study performed by Junior et al. (2009) shows that at different values of resistance the maximum tip displacement occurs at different frequency values as shown in Figure 3.17. Hence it can be concluded that one of the reasons for the peak voltage to occur at different frequencies in the model and experiment could be that the value of resistance used is the not optimal one.

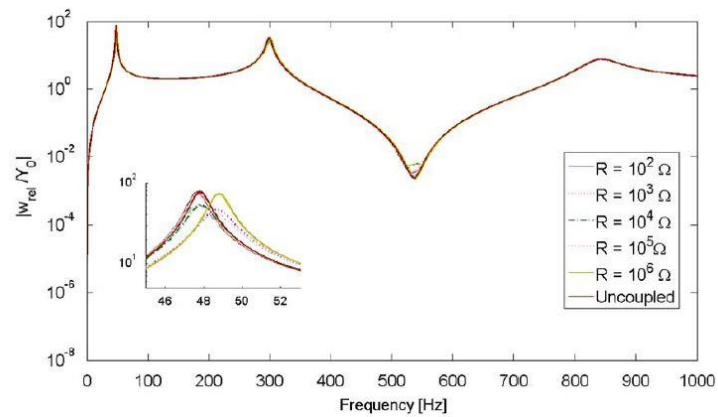


Figure 3.17 Variation of tip displacement versus frequency for different resistance (Junior et al., 2009)

3.5. Conclusion

In conclusion, although there are certain discrepancies between the model and the experiment, the errors are small. One approach would be to correct the model, based on the various factors discussed in Section 3.4, to obtain a closer match with the experiments. However, the purpose of developing a model was to use it further for performing optimization studies. Since the overall trend and values of voltage versus frequency were acceptable, the current model was treated as a preliminary model and was assumed to be validated appropriately with the performed experiments. This model was used for optimizing the shape of the beam and the patch, as discussed in Chapter 4.

4. Optimization

After the mathematical model developed in Matlab was validated against an experiment the next step was to perform the shape optimization of the model in Matlab. This chapter will contain the main novelty of this thesis which will be the setup of the shape optimization of the energy harvesters with a microfiber composite. Shape optimization is extremely challenging and computationally expensive when compared to sizing optimization. The reason for this is that when shape optimization is performed the program has to perform multiple evaluations of the objective function and design variable before one iteration is complete and multiple iterations have to be performed before optimized values are reached. For this thesis, the objective was to maximize the voltage and to obtain the voltage several terms needed to be calculated (shown in Equations (32) – (37) and (43)), this also made the problem computationally quite expensive. Given all the challenges involved in shape optimization, it is generally avoided in any structural optimization problem.

Chapter 4 will have three sections which will be sensitivity analysis, a two design variable case and a three design variable case. The two design variable case will be further divided into two sections, one for the length of the beam (L_B) and the length of the patch (L_P) and the other for the length of beam (L_B) and delta (δ). The three design variable case will combine all the design variables discussed in the two variable case, i.e. the length of the beam (L_B), the length of the patch (L_P) and delta (δ).

4.1. Sensitivity Analysis

Sensitivity analysis is a study of “how much” and “how” the objective function changes in response to changes in certain parameters. Since shape optimization will be

performed on the beam it is extremely important to understand the effect each of these parameters have on the objective function which in this case will be the harvested voltage. The different methods for sensitivity analysis is shown in Figure 4.1.

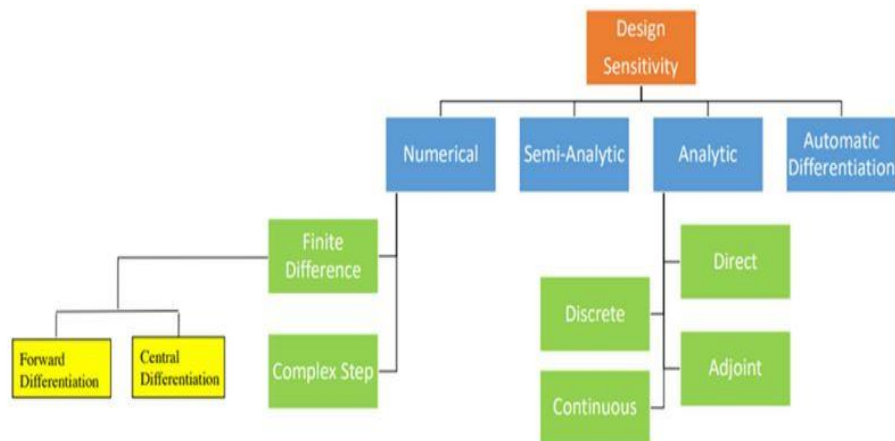


Figure 4.1 Flowchart of different sensitivity analysis methods

Numerical methods like complex step and finite difference are computationally expensive though they are easy to implement. The complex step method requires the analysis code to handle complex number arithmetic which is not always available (such as for analysis done using Nastran or Ansys), and it may also require more computational memory per iteration than the other methods. Analytical methods have higher accuracy compared to numerical methods which makes them more desirable to implement. Also in analytical methods, the need for convergence of the right step size (as required for finite difference method) or involvement of complex numbers doesn't exist. Though it is highly desirable to use the analytical method for step size calculation for the reasons stated above, its implementation is quite intricate and with the presented detailed model for the energy harvester, these are out of scope for this thesis. In this thesis, we would like to

create a simple optimization process that is not only easier to understand but also easier to implement. A brief description of a few methods is discussed below with an example frequency sensitivity with respect to the length of a simple cantilever beam.

4.1.1. Finite Difference Method

This method is a numerical design sensitivity analysis (DSA) method. Though the accuracy maybe slightly lower using this method it is quite easy and simple to implement and is also used quite commonly. To obtain the sensitivity using this method the function whose sensitivity is required is calculated at two different values, one the actual value at the original parameters and the other with a small increment in the step size of the parameter with respect to which the sensitivity is required. The difference between the two calculated values divided by the step size would give us the sensitivity. In this case, frequency sensitivity with respect to the length of the beam is calculated which can be represented mathematically as shown below,

$$\dot{\omega} = \frac{\omega(L+dL) - \omega(L)}{dL} \quad (57)$$

Where $\dot{\omega}$ is the frequency sensitivity with respect to the parameter (length of the beam in this case), $\omega(L + dL)$ is the frequency calculated at the step size increment, $\omega(L)$ is the frequency at the original parameters and dL is the step size. Finite difference method suffer from two major types of errors the round-off error and truncation error. Theses error will be explained with respect to a figure of the frequency sensitivity with different step sizes. Using (57) frequency sensitivity was calculated with respect to different step sizes of step length 10^{-n} where n was varied from 1 to 11. A plot of the log of step versus log of the error calculated from the exact value is shown in Figure 4.2. It can be seen that the best step size for this particular case is 10^{-7} but it could be different for a different

problem. Hence selection of the best step size could be a computationally expensive task. Also from the Figure 4.2, it can be seen that if the step size is too small it could lead to round-off errors while if the step size is too large it could lead to truncation errors. It should be mentioned that these errors are quite small but it is always desirable to have the least amount of errors possible.

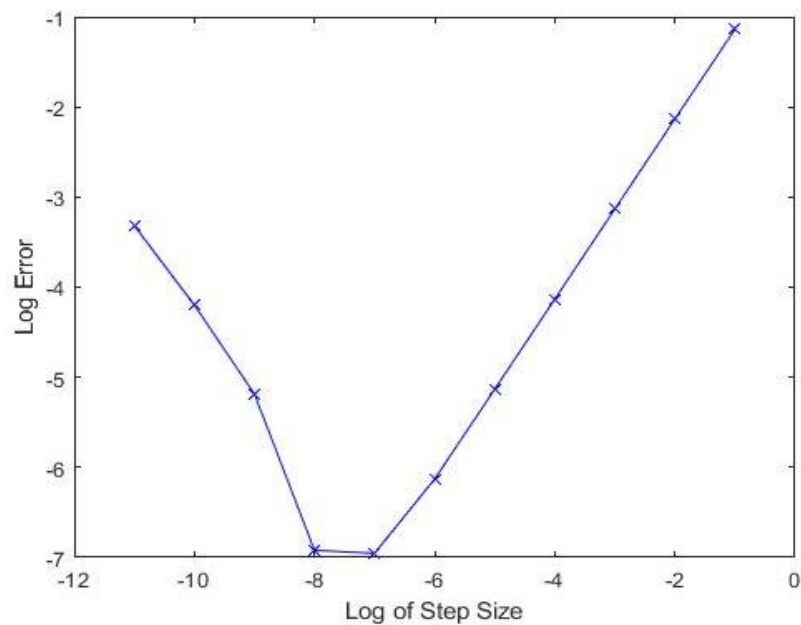


Figure 4.2 Plot of log of step size versus log of error

4.1.2. Complex Step

Another numerical DSA method is the complex step method. The total design derivative is numerically approximated where i is the imaginary number $\sqrt{-1}$ as seen in (58). The complex step method and the finite difference method are quite similar since both suffer from truncation errors in larger step size but differ in smaller step size where complex step doesn't result in round-off error the for smaller step size. This is due to the fact that there is an absence of a subtractive operation and this can be numerically exact

for the smaller step size. Hence, the arbitrarily smaller step size can be chosen for this method. The problem with complex step arises when the analysis has to be done using complex numbers for step size, which is not feasible in most commercial software packages.

$$f'(x) = \frac{\text{Im } g[f(x + ih)]}{h} \quad (58)$$

4.1.3. Discrete Analytical

To formulate the equations for discrete analytic method knowledge of governing equations is required. These governing equations first need to be discretized and, then to be differentiated. For the frequency sensitivity the discretized, linear static version equation is shown in (59), where $[K]$ is the stiffness matrix, $[M]$ is the mass matrix $\{\phi\}$ is the vector for mode shape and λ is the eigenvalue. Differentiating equation with respect to a shape parameter 'x' yields the discrete analytical sensitivity equations shown in (60). Upon solving equation (60), λ' contains the discrete values of frequency derivatives of the field variables at finite element nodes.

$$[K]\{\phi\} = \lambda[M]\{\phi\} \quad (59)$$

$$\lambda' = \phi^T ([K'] - \lambda[M'])\{\phi\} \quad (60)$$

4.1.4. Exact or Analytical

As the name suggests for this method an exact solution is required. To obtain the sensitivity through this method, we differentiate the equation with respect to the variable whose sensitivity is required. Though implementation of this may be quite easy to obtain the exact solutions for certain problems is a computationally expensive method especially when 2D and 3D problems are involved. For the example of a cantilever beam natural frequency, the exact solution is shown in (61).

$$\omega_n = (\lambda L) \sqrt{\frac{EI}{mL^4}} \quad (61)$$

Differentiating the above frequency equation with respect to the length 'L' will give us the exact solution for frequency sensitivity shown in (62),

$$\dot{\omega}_{nL} = \frac{-2(\lambda L)}{L^3} \sqrt{\frac{EI}{m}} \quad (62)$$

In order to compare the frequency derivatives from the methods mentioned above, the dimensions and properties of the beam used are shown in Table 4.1. All the frequency derivatives are with respect to increasing length of the beam keeping everything else constant. A comparison of the frequency sensitivity of the first three natural frequencies of a cantilever beam as shown in Table 4.2.

Table 4.1

Properties and dimensions of the cantilever beam

Properties / Parameters	Values
Density (ρ)	2700 kg/m ³
Young's Modulus (E)	69 GPa
Length	10 m
Width	5 m
Height	3 m

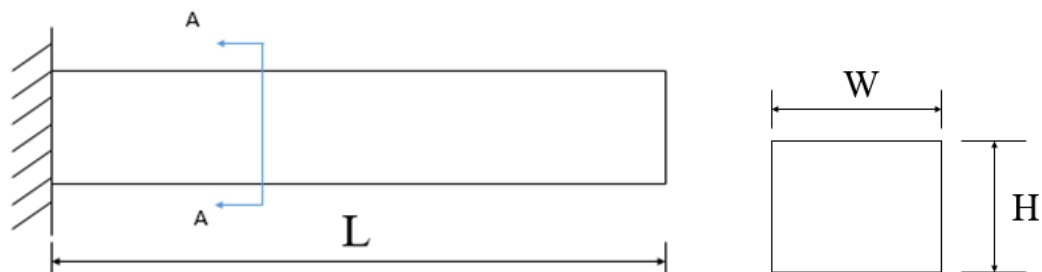


Figure 4.3 Cantilever beam setup and beam cross section

Table 4.2

Comparison of frequency sensitivity using different methods

Mode number	Finite difference	Analytical	Discrete analytical (MSC Nastran)
1	-4.8998	-4.8998	-4.8941
2	-30.7058	-30.7062	-30.584
3	-85.9770	-85.9783	-85.419

As can be seen from Table 4.2 all the different methods have an excellent correlation with each other. In this research, Matlab's predefined FMINCON function will be used for optimization which uses finite difference for its sensitivity analysis.

4.2. Two Variable Optimization

The mathematical model developed in the previous chapters of thesis was used to perform the shape optimization of the energy harvester. In this section we will discuss two cases for the shape optimization of the beam, each having two shape variables, as follows:

- The first case will be the optimization of the length of the beam (L_B) and length of the patch (L_P) which will be the constant width case.
- The second case will include a varying width of the beam. The width will be varied using an exponential parameter δ . In that case, optimization will be performed for the length of the beam (L_B) and δ .

For both the cases the objective function will be the minimization of negative of voltage ($-V$) which is the same as maximization of the voltage (V). The constraint were mainly kept for the value of the dimensional parameters. A design space plot will be plotted and optimization will be run to check if the design space plot and optimization

follow the same trend. Figure 4.4 shows the different design variables used for the shape optimization problem. The parameter δ defines how the width of the beam w_b varies along the length of the beam.

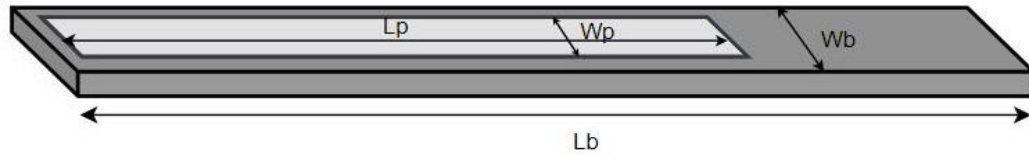


Figure 4.4 Different design variables for the shape optimization problem

4.2.1. Length of Beam and Length of Patch Case

In this case length of the beam (L_B) and length of the patch (L_P) were the design variables, with their limits being $160e-3$ to $350e-3$ and $10e-3$ to $150e-3$ respectively. The formulation of the optimization process is shown below,

$$\text{Min } V(L_B, L_P) = -v \quad (63)$$

Where,

$$v = \left(\frac{\Theta R F}{\sqrt{2} M} \right) \frac{1}{\sqrt{\left(\left(\frac{\Theta^2 R}{M} + C_p R (\omega_n^2 - \omega^2) + 2\zeta \omega_n \right)^2 + \left(\frac{\omega_n^2}{\omega} - \omega - 2\zeta \omega \omega_n C_p R \right)^2 \right)}} \quad (64)$$

Subject to,

$$160e-3 < L_B < 350e-3 \quad (65)$$

$$10e-3 < L_P < 150e-3 \quad (66)$$

$$M = M_B(L_B) + M_P(L_P) \quad (67)$$

$$\mathbf{K} = \mathbf{K}_B(L_B) + \mathbf{K}_P(L_P) \quad (68)$$

$$\Theta = \Theta(L_P) \quad (69)$$

$$\mathbf{F} = \mathbf{F}(L_B, L_P) \quad (70)$$

The objective function of this optimization case is shown in (63) which is the minimization of the negative of the voltage where voltage can be obtained from (64). The constraints are shown in (65) and (66). It can be seen from (64) that voltage doesn't explicitly depend on the L_B and L_P but can be related to each other through the mass matrix, stiffness matrix, electromechanical coupling term and force term shown in (67), (68), (69) and (70) respectively (The previously stated terms have been defined in Chapter 2 of this thesis – refer Equations 32 – 37 and 43). Before the optimization problem was executed on Matlab a design space was plotted for L_B , L_P , and voltage and is shown in Figure 4.5, the contour lines on the graph are the values of the objective function (voltage). This was done since the optimization case considered here is an easy two design variable problem and it was possible to have a design space. The design space served as verification if the FMINCON solution is reasonably accurate because a comparison can be made between the two. It can be seen that the voltage increases with an increase in the length of the beam but there is no linear relationship between the voltage and length of the patch L_P .

After setting up the optimization problem, the FMINCON function in Matlab was used to perform the shape optimization. Three different algorithms were used with the fmincon function of Matlab, which were active-set, SQP, and interior-point. The path followed by each algorithm is shown in Figure 4.6. As can be seen, that though each

algorithm follows a different path all of them converge to the same point on the design space which is the point of the maximum voltage.

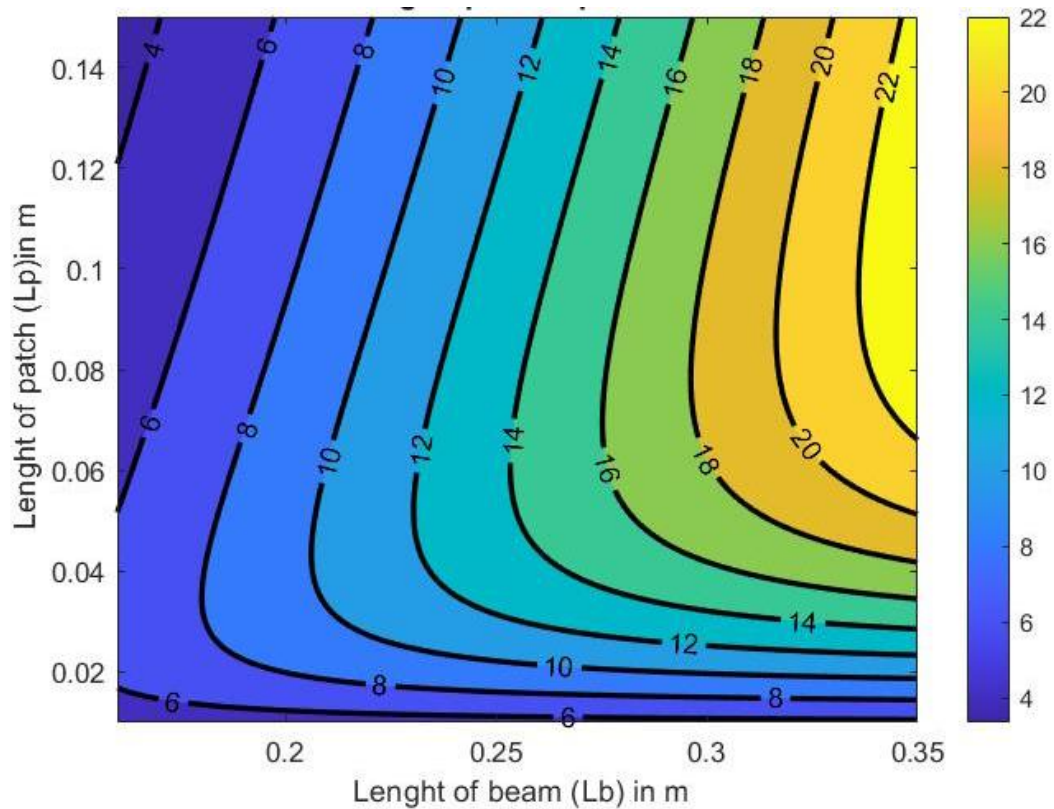


Figure 4.5 Design space for length of the beam (L_B) and length of the patch (L_P)

The number iteration taken by each algorithm versus the objective function value is shown in Figure 4.7. From Figure 4.7 it can be seen the number of iterations needed to reach the same objective function is least for active set, followed by SQP, and interior-point takes the most number of iterations. Another comparison needs to be made for the different algorithms is the first order optimality. This number should be as close to zero as possible. This is a necessary condition for a minimum point. If the first-order optimality is not zero or close enough to zero at the stopping point of the objective function it may not be a minimum and that would not be an optimum point.

A plot of the number of iteration versus the first-order optimality for the different algorithms is shown in Figure 4.8. It can be seen that for each iteration case the value of the first-order optimality reaches zero before the optimization stop and therefore it can be concluded that each algorithm reaches a minimum point. The different values of the objective function and design variables for each iteration are shown in the tables below. It can be concluded that best first order optimality value is obtained from the interior point algorithm while the active-set algorithm has the highest value for the first order optimality. This trend is reversed compared to that of the number of iteration taken by these algorithms respectively.

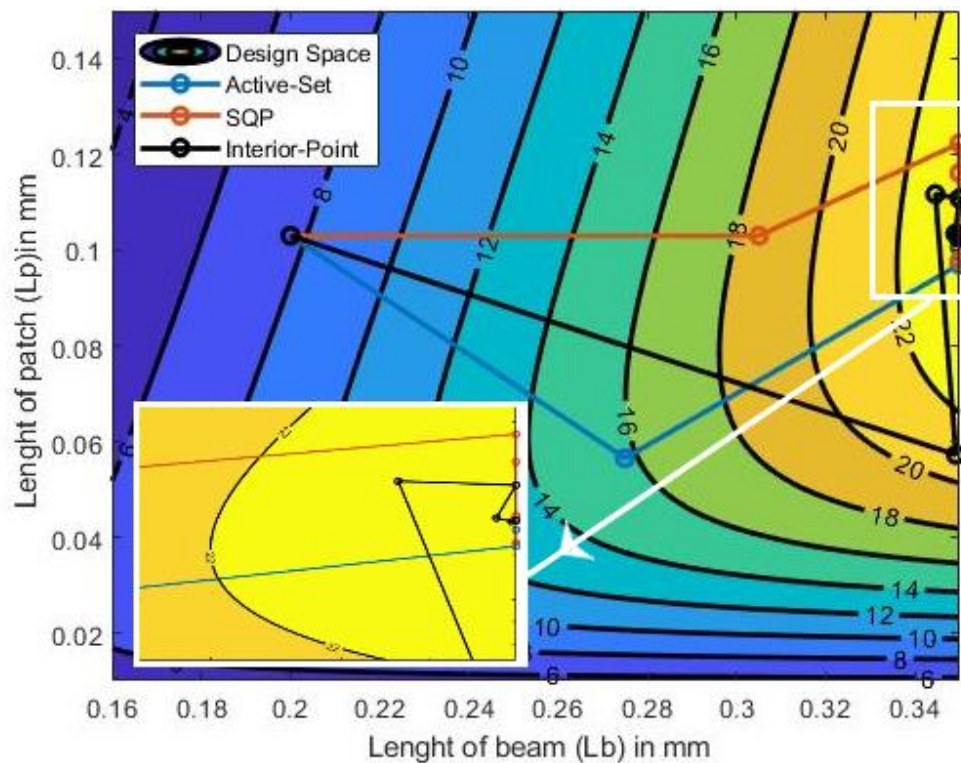


Figure 4.6 Optimization paths for the L_B and L_P case

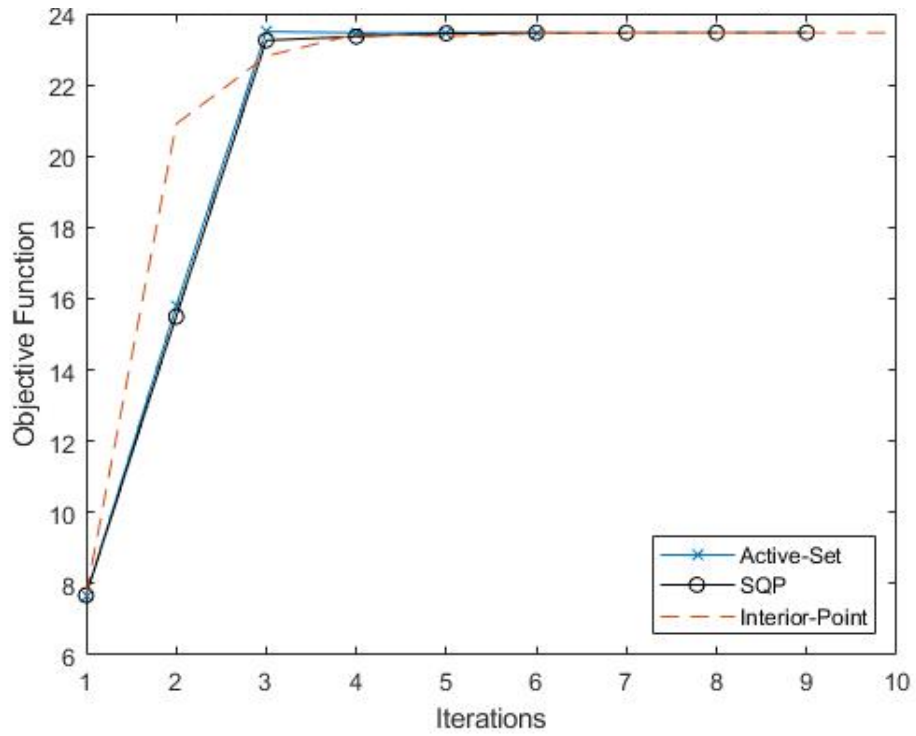


Figure 4.7 Iteration versus objective function for the L_B and L_P case.

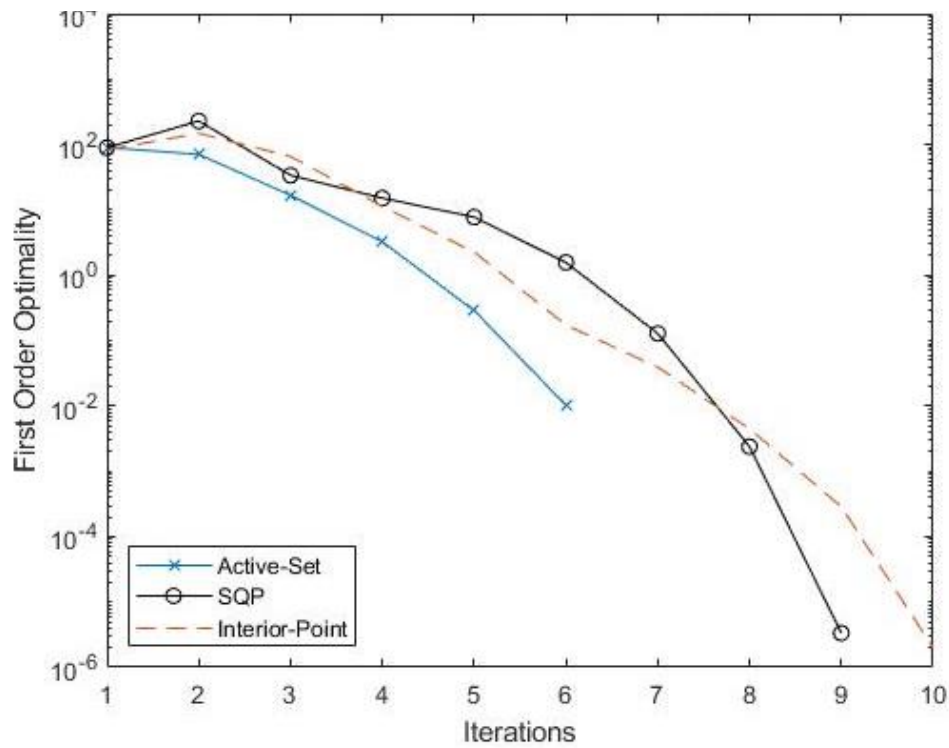


Figure 4.8 Iterations versus first order optimality for the L_B and L_P case

Table 4.3

Iterations and values of L_B and L_P for the active-set algorithm

Iteration	Objective function – voltage (V)	Length of beam(L_B) – m	Length of patch(L_P) – m	Reason for FMINCON stop
1	-7.67433	0.2000	0.103	Predicted change in the objective function is less than the value of the function tolerance and constraints are satisfied to within the value of the constraint tolerance.
2	-15.7701	0.2750	0.0565	
3	-23.4392	0.3500	0.0970	
4	-23.4617	0.3500	0.1007	
5	-23.4653	0.3500	0.1027	
6	-23.4653	0.3500	0.1029	

Table 4.4

Iterations and values of L_B and L_P for the SQP algorithm

Iteration	Objective function – voltage (V)	Length of beam(L_B) – m	Length of patch(L_P) – m	Reason for FMINCON stop
1	-7.674427	0.2	0.130	Objective function is non-decreasing in feasible direction, to within the value of the optimality tolerance, and constraints are satisfied to within the value of the constraint tolerance.
2	-15.49344	0.305	0.0379	
3	-23.24810	0.35	0.1223	
4	-23.35798	0.35	0.1161	
5	-23.44615	0.35	0.0978	
6	-23.46440	0.35	0.1040	
7	-23.46529	0.35	0.103	
8	-23.46530	0.35	0.1029	
9	-23.46530	0.35	0.1029	

Table 4.5

Iterations and values of L_B and L_P for the interior-point algorithm

Iteration	Objective function – voltage (V)	Length of beam(L_B) – m	Length of patch(L_P) – m	Reason for FMINCON stop
1	-7.674427	0.2	0.103	Objective function is non-decreasing in feasible direction, to within the value of the optimality tolerance, and constraints are satisfied to within the value of the constraint tolerance.
2	-20.89671	0.3492	0.0572	
3	-22.80829	0.3446	0.1117	
4	-23.42219	0.3500	0.11080	
5	-23.36578	0.3491	0.1034	
6	-23.44351	0.3498	0.1026	
7	-23.46512	0.3500	0.1029	
8	-23.46510	0.3500	0.1029	
9	-23.46529	0.3500	0.1029	
10	-23.46529	0.3500	0.1029	

From Table 4.3, Table 4.4 and Table 4.5 it can be seen that all the algorithm converge to the same values of the design variables. Each algorithm has a difference in the number of iterations required to reach that point.

4.2.2. Length of Beam and Delta (δ) Case

The case was run after the implementation of the necessary changes discussed in section 2.5 of this thesis. The design variables, in this case, were L_B and delta (δ) with limits being $150e-3$ to $350e-3$ mm and -1 to 1 respectively. The formulation of the optimization problems is shown below,

$$\text{Min } V(L_B, \delta) = -V \quad (71)$$

Subject to,

$$150e-3 < L_B < 350e-3 \quad (72)$$

$$-1 < \delta < 1 \quad (73)$$

$$M = M_B(L_B, \delta) + M_P \quad (74)$$

$$K = K_B(L_B, \delta) + K_P(L_P) \quad (75)$$

$$F = F(L_B, \delta) \quad (76)$$

Just like the previous case the optimization objective function for this case was also minimization of the negative of voltage as shown in (71), which can be obtained from (64). The constraints, in this case, were the limits on the design variables L_B and δ as shown in (72) and (73) respectively. In case as well there isn't an explicit between the voltage and design variables but can be related to each other through the Equations specified from 74 – 76. Since this is a varying width problem the necessary changes to mode shapes, the width of the beam (w_B), mass matrix, stiffness matrix, and force were made as stated in section 2.5. Being a two-variable optimization problem it was again possible to obtain the design space in this case as well for the same reason as the ones stated for the previous case. The design space is shown in Figure 4.9 in which the contour lines are the values of voltages corresponding to the respective set of design variables.

From Figure 4.9 it is seen that the length of beam and objective function (voltage) have a linear relationship which is similar to the one stated in the previous case. With delta (δ), it can be seen that for positive values of δ the voltage increases and for negative values of δ the voltage decrease. In other words, the voltage increase for a reverse taper i.e. increasing width from the base the voltage increase and decrease for a decreasing width profile.

After obtaining the design space plot, a similar optimization was run using the FMINCON command in Matlab with the objective function being the minimization of voltage and the constraints on the design variables being the same values of L_B and δ as soon in the design space plot. The same three algorithms were chosen as before i.e. active set, SQP, and Interior-point. The optimization path for all three algorithms is shown in Figure 4.10. It is seen that again all three algorithms converge to the same point on the design space though they take slightly different paths. Note that in the figure the path for Active set and SQP overall and hence it is difficult to differentiate between the two.

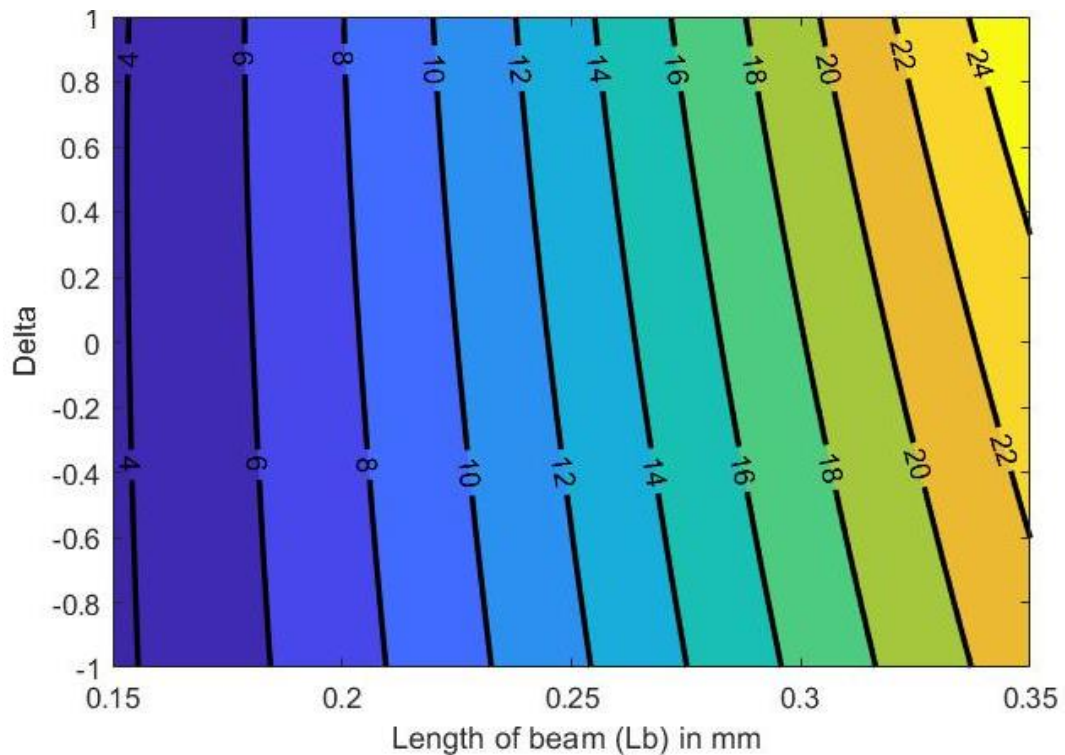


Figure 4.9 Design space for length of the beam (L_B) and width varying parameter delta (δ)

Iteration versus objective function and iteration versus first-order optimality for this case is shown in Figure 4.11 and Figure 4.12 in respectively. It is seen that the active-set

algorithm takes the least almost of iterations and interior-point takes the maximum number of iteration between the three algorithms. From the first-order optimality, it is seen that for active-set when the optimization stops the first order-optimality is only 10.1 which is not desirable but for SQP and interior-point the first-order optimality is very close to zero. For both these algorithms the same value of the objective function and design variables is obtained as for active-set. Therefore it can be safely concluded that though the first order-optimality is quite high for active set the optimized voltage and design variables are the desired value. Another important point to be mentioned is that the objective function and design variables reach the same point as indicated in the design space plot.

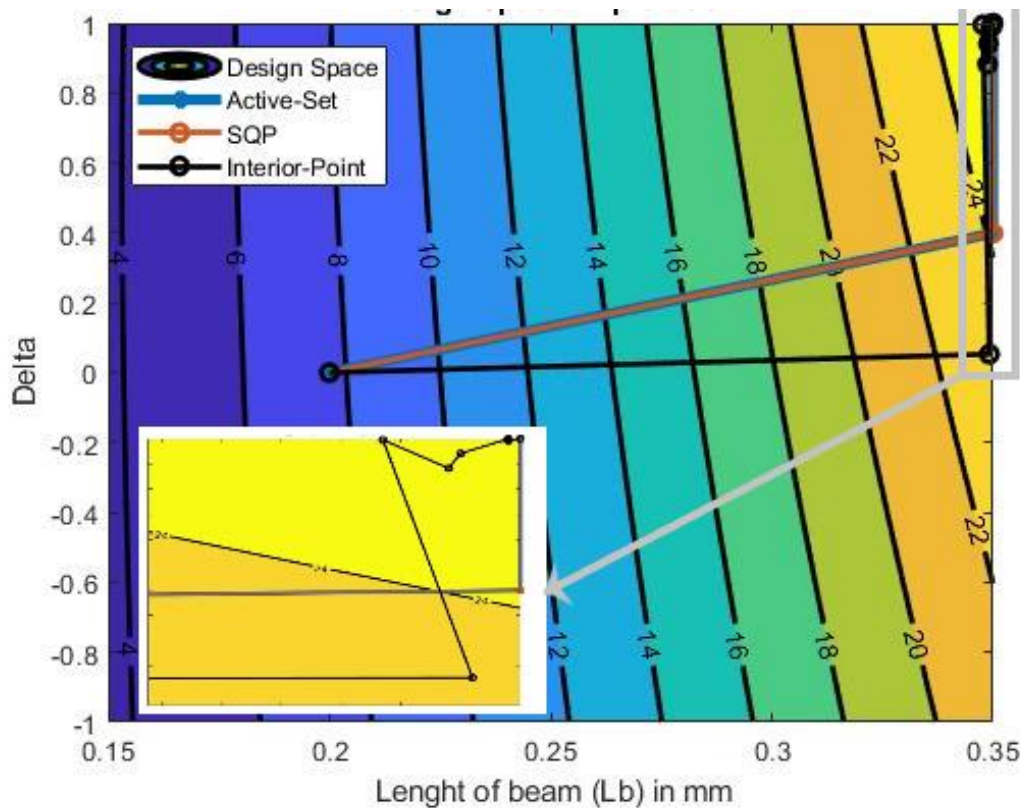


Figure 4.10 Optimization paths for the L_B and δ case

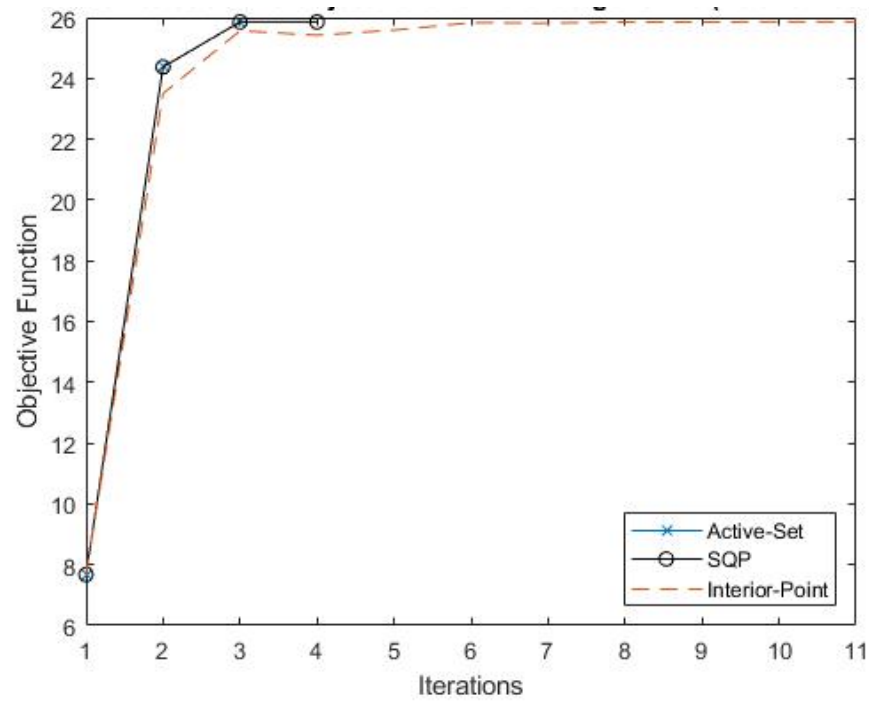


Figure 4.11 Iterations versus objective function for the L_B and δ case

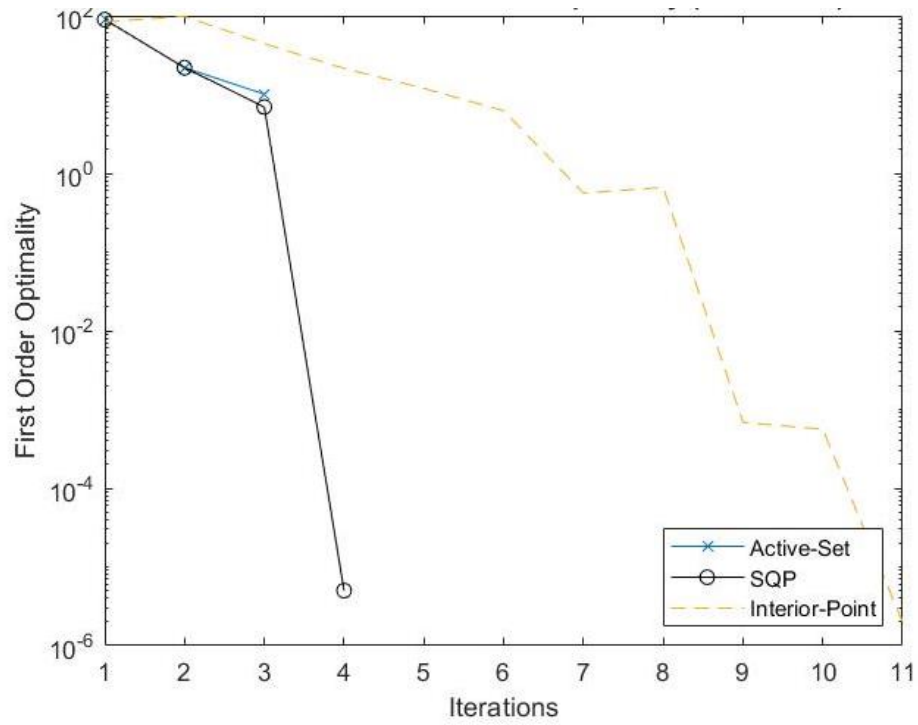


Figure 4.12 Iterations versus first order optimality for L_B and δ case

The different values of the objective function and design variables for each iteration are shown in the tables below. The same three algorithms were used as the previous case.

Table 4.6

Iterations and values of L_B and δ for the active-set algorithm

Iteration	Objective function – voltage(V)	Length of beam(L_B) – m	Delta (δ)	Reason for FMINCON stop
1	-7.67443	0.2	0	Objective function is non-decreasing in feasible direction, to within the value of the optimality tolerance, and constraints are satisfied to within the value of the constraint tolerance
2	-24.377	0.35	0.3991	
3	-25.858	0.35	1	

Table 4.7

Iterations and values of L_B and δ for the SQP algorithm

Iteration	Objective function – voltage (V)	Length of beam(L_B) – m	Delta (δ)	Reason for FMINCON stop
1	-7.674427	0.2	0	Objective function is non-decreasing in feasible direction, to within the value of the optimality tolerance, and constraints are satisfied to within the value of the constraint tolerance
2	-24.37586	0.35	0.3991	
3	-25.85805	0.35	1	
4	-25.85805	0.35	1	

Table 4.8

Iterations and values of L_B and δ for the interior point algorithm

Iteration	Objective function – voltage(V)	Length of beam(L_B)-m	Delta (δ)	Reason for FMINCON stop
1	-7.674427	0.2	0	Objective function is non-decreasing in feasible directions, to within the value of the optimality tolerance, and constraints are satisfied to within the value of the constraint tolerance
2	-23.50323	0.3492	0.0530	
3	-25.56723	0.3477	0.9953	
4	-25.42021	0.3488	0.8830	
5	-25.58858	0.3490	0.9412	
6	-25.83331	0.3498	0.9997	
7	-25.81815	0.3498	0.9921	
8	-25.85752	0.350	0.9999	
9	-25.85765	0.350	0.9999	
10	-25.85804	0.350	1	
11	-25.85804	0.350	1	

From Table 4.6, Table 4.7 and Table 4.8 it is seen that though the number of iterations are different, mainly for interior-point the end point for the optimization for the different algorithms is the same. Also, it can be seen that by using a tapered beam the voltage value obtained after optimization is more compared to the ones obtained in the previous case (L_B and L_P case). Hence an optimized shape would be a reverse taper beam compared to a constant cross section.

4.3. Three Variable Optimization

In this section, optimization was performed which combined the two cases discussed in the previous section for the same objective function. The design variable were the length of the beam (L_B), the length of the patch (L_P) and delta (δ). The setup of the optimization problem for this case is shown below,

$$\text{Min } V(L_B, L_P, \delta) = -V \quad (77)$$

Subjected to,

$$160e-3 < L_B < 350e-3 \quad (78)$$

$$10e-3 < L_P < 150e-3 \quad (79)$$

$$-1 < \delta < 1 \quad (80)$$

$$M = M_B(L_B, \delta) + M_P(L_P) \quad (81)$$

$$K = K_B(L_B, \delta) + K_P(L_P) \quad (82)$$

$$\Theta = \Theta(L_P) \quad (83)$$

$$F = F(L_B, L_P, \delta) \quad (84)$$

The objective function in this case is the same as the previous two cases (minimization of the negative voltage) described in (77) with the constraints being limits on the design variables L_B , L_P and δ shown in (78), (79) and (80) respectively. The voltage has an implicit relation to the design variables shown (81) - (84). In this case, it was not possible to obtain a design space plot since there are three design variables and an objective function that would require a 4-D plot. The optimization in the two variable case helped in identifying the possible trends for the objective function. The trends obtained in the two design variable case would serve as a verification if similar trends are obtained for the three design variable case as well.

Optimization was performed using the FMINCON function in Matlab for the objective function shown in (77) with the constraints (78), (79) and (80). The same three algorithms were used as in the previous cases. Figure 4.13 shows the path followed by different algorithms. Similar to the previous cases, in this case as well all the algorithms

converged to the same point, though the path taken by them are slightly different with the increasing number of iterations being for active-set, SQP and interior point. Figure 4.14 shows the number of iterations taken for each algorithm to reach the optimum point. The first order optimality in this problem was close enough to zero (Figure 4.15) for all the three algorithm which is the desirable value for it, hence it can be said that the convergence of all the algorithms is quite good. As for the results the length of the beam (L_B) as well as delta (δ) always tend towards the upper limit of the constraints while the length of the patch (L_P) decreased slightly from 0.103 m to 0.1015 m. These trends are quite similar to the ones obtained for the two design variable cases.

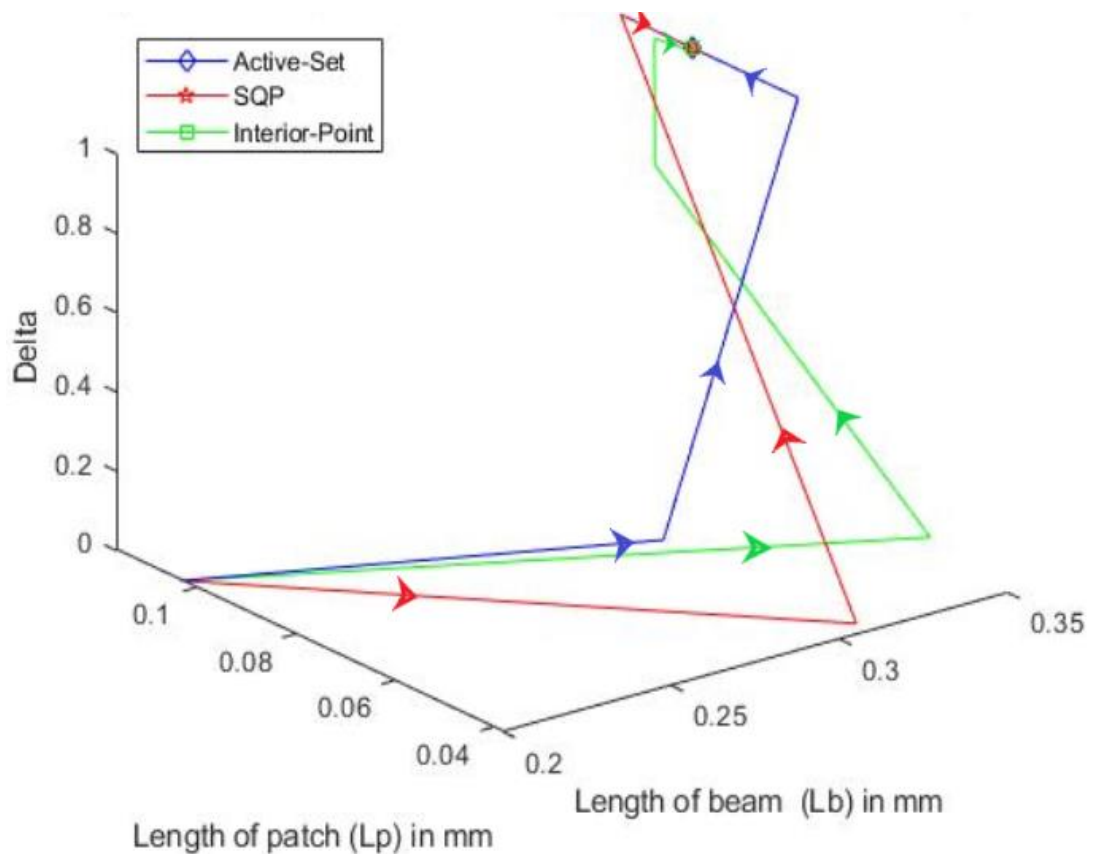


Figure 4.13 Optimization paths for the three design variable case

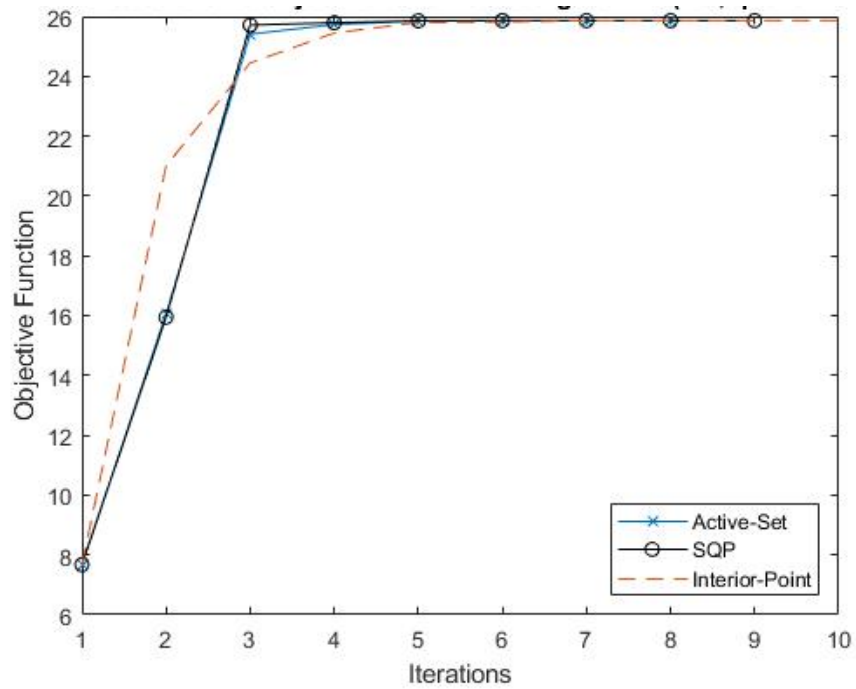


Figure 4.14 Iterations versus objective function for the three design variable case

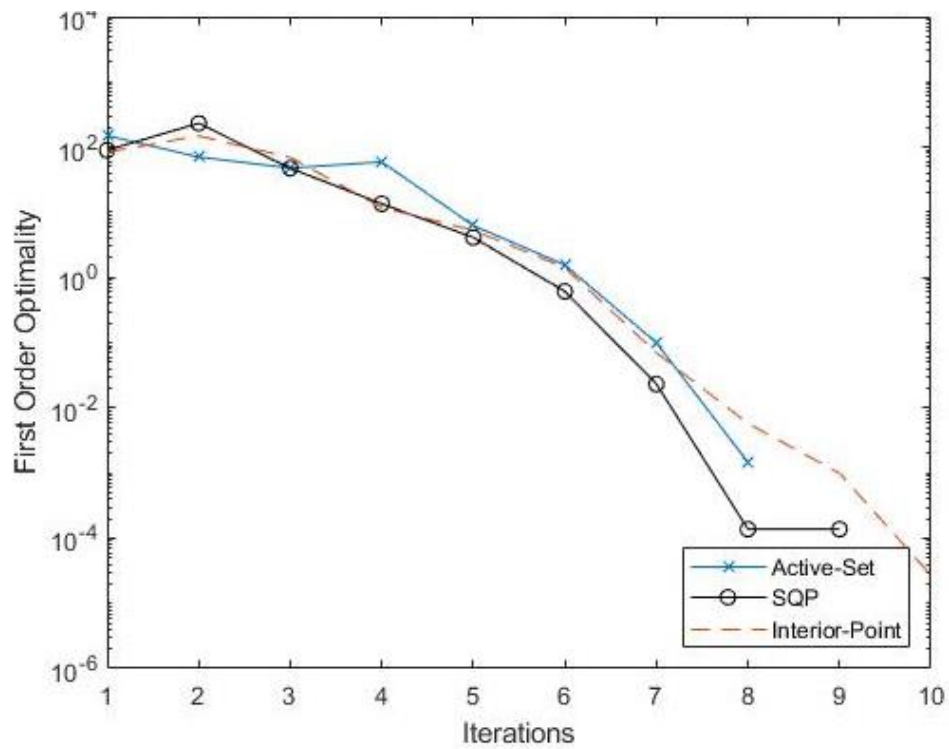


Figure 4.15 First order optimality for the three design variable case

Table 4.9

Iterations and values of L_B , L_P and δ for the active-set algorithm

Iteration	Objective function – voltage (V)	Length of beam(L_B) - m	Length of patch(L_P) - m	Delta (δ)	Reason for FMINCON stop
1	-7.67433	0.2	0.103	0	The size of the current search direction is less than twice the value of the step size tolerance constraints are satisfied to within the value of constraint tolerance
2	-16.0539	0.2750	0.0565	0.1996	
3	-25.4088	0.35	0.0802	1	
4	-25.7302	0.35	0.1151	1	
5	-25.8466	0.35	0.1056	1	
6	-25.8592	0.35	0.1005	1	
7	-25.8599	0.35	0.1015	1	
8	-25.8599	0.35	0.1015	1	

Table 4.10

Iterations and values of L_B , L_P and δ for the SQP algorithm

Iteration	Objective function – voltage (V)	Length of beam(L_B) – m	Length of patch(L_P) - m	Delta (δ)	Reason for FMINCON stop
1	-7.674427	0.2	0.103	0	The size of the current step is less than the value of the step size tolerance and constraint are satisfied to within the value of the constraint tolerance
2	-15.94737	0.305	0.0379	0.02794	
3	-25.71365	0.35	0.1160	1	
4	-25.79049	0.35	0.1113	1	
5	-25.85490	0.35	0.0990	1	
6	-25.85980	0.35	0.1018	1	
7	-25.85992	0.35	0.1015	1	
8	-25.85992	0.35	0.1015	1	
9	-25.85992	0.35	0.1015	1	

Table 4.11

Iterations and values of L_B , L_P and δ for the interior-point algorithm

Iteration	Objective function – voltage (V)	Length of beam(L_B) - m	Length of patch(L_P) - m	Delta (δ)	Reason for FMINCON stop
1	-7.674427	0.2	0.103	0	The objective function is non-decreasing in feasible directions, to within the value of the optimality tolerance and constraints are satisfied to within the value of the constraint tolerance
2	-21.00686	0.3492	0.0572	0.0530	
3	-24.44667	0.3446	0.1054	0.6950	
4	-25.44772	0.3469	0.1071	0.9985	
5	-25.79950	0.3498	0.1049	0.9875	
6	-25.82014	0.3498	0.1021	0.9923	
7	-25.85916	0.35	0.1014	0.9999	
8	-25.85952	0.35	0.1015	0.9999	
9	-25.85991	0.35	0.1015	1	
10	-25.85991	0.35	0.1015	1	

From Table 4.9, Table 4.10 and Table 4.11 it can be seen that the same trend is followed as the previous two cases where active-set takes the least number of iterations and interior point the maximum number of iterations. Also all the algorithms converge to the same point. Therefore it can be concluded that the setup of the shape optimization works well with the defined problem and can be applied to more complicated cases which could include more than three design variables.

4.4. Conclusion

In this chapter, a brief discussion of sensitivity analysis was made followed by an explanation of a few methods for performing sensitivity analysis along with the advantage and disadvantages for each. A cantilever beam was used as an example to perform frequency sensitivity with respect to the length of the beam to differentiate from

the different methods. It was seen that all three methods gave extremely similar results. After sensitivity analysis, optimization of the two design variable case was discussed with different algorithms using Matlab's FMINCON function. In all the optimization cases using FMINCON, a finite forward difference method was used to perform sensitivity analysis and a step size of square root of eps was used, where the value for eps was $2.2204e-16$. For the first case in the two design variable section, a constant width beam was used while for the second case a varying width beam was used. The results for both the cases converged well for all the three algorithms. Finally a three design optimization for performed for L_B , L_P , and δ . In all the optimization cases active-set algorithm took the least number of iterations and interior-point took the most number of iterations, though all the algorithms converged to the same point even with thought the number of iterations varied for each algorithm.

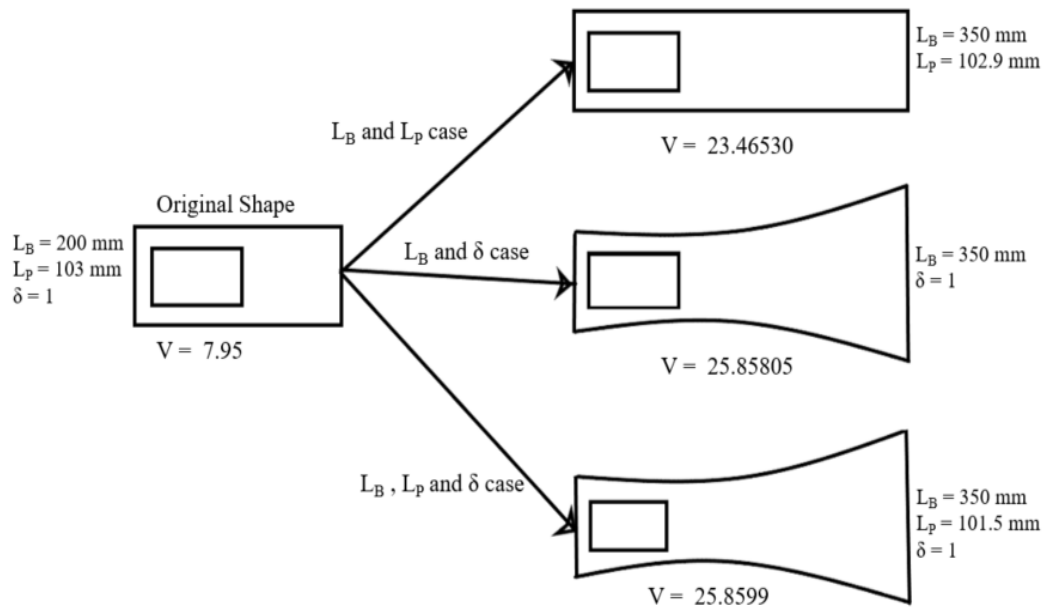


Figure 4.16 Final optimization shapes for the different cases

Also an optimization problem was setup which is not only easy to understand but also easy to implement. An exponentially varying width was implemented which has not been done before up to the author's knowledge. Also, the implementation of such a three design variable optimization hasn't been performed before. This also serves as a base to perform much more complex optimization, one of which can be the addition of more design variables. Though the constraints were more open-ended than what was initially thought, much more complex constraints can be added to the problem depending on the needs of the user.

5. Conclusions, Recommendation and Future Work

In this thesis, a mathematical model for an energy harvester beam with a unimorph configuration was setup on Matlab. This model was based upon multiple studies/researches done towards modeling of energy harvester with a piezoelectric type of material used for energy harvesting application. The piezoelectric material used in this study was a Microfiber composite which is extremely flexible and was developed at NASA's Langley research center.

5.1. Conclusion

Once the mathematical model was developed based on the governing set of equations for an electromechanical coupled system, it was validated against an experiment. An FRF was performed to determine the approximate frequency for which the experiment should be performed and also the simulated frequency range which would be the same as the range at which the experiment was performed. It was found from the experimental FRF that the first bending mode was 27.4 Hz. Hence a frequency range for 21-31 Hz was used to accommodate for error. It was observed that there was a slight discrepancy between the experiment and the model for the output voltage. From the experiment, the peak voltage was observed at 25 Hz while for the experiment it was observed at 28 Hz. The peak voltage is always assumed to occur at the first natural bending frequency because it is the point of the high stress value.

The discrepancy in the peak voltage occurring at different frequencies could be due to a few reasons, (a) the force input to the numerical model is based on the reading of acceleration at the base of the energy harvester beam and this approximation may have resulted in a poor match between the experiment and the model, (b) the correct value of

damping wasn't used, (c) the model accommodates for only the first mode, using a model which accommodates for more number of modes could give more accurate results, and (d) the value of resistance used may not be the optimal one and therefore by using an optimal value of resistance may results in lesser discrepancy. Though there was a small difference in the frequency at which the peak voltage was obtained from the experiment and model, they both had the same value of the maximum voltage generated and also followed the same trend. Hence, it was concluded that the model was good enough to perform optimization on it.

After the model validation was done an optimization problem was set up for different cases where the objective function for each case for the minimization of negative of the voltage and the constraints on the design variables were arbitrary parameters chosen at random. The main reason for choosing random parameters was to check if the optimization followed the same trend as expected. The expected trend was obtained by plotting a design space if it was possible. A two variable and three variable optimization was performed. For two design variables, it was easy to plot a design space and the optimization followed the design space plot as expected.

For a three design variable case, a design space wasn't possible but the trends were similar to the previous cases, i.e. the voltage increased with an increase in L_B and increased for positive values of δ , there was no direct relation found between the length of the patch L_P and voltage (the length of patch was always near to the original value). This study may be used to perform a more detailed shape optimization of the energy harvester based upon more realistic design requirements. The design requirements will be based on the application of the user.

5.2. Knowledge Gained and Challenges Tackled

The following were some of the different challenges tackled and knowledge gained throughout this thesis:

- It was extremely difficult to obtain a perfect model validation with the experiment. There were a lot of factors to be taken into consideration which would affect the model validation which made the process extremely challenging.
- Setting up of the experiments for the energy harvester as well as parameter identification were challenging. Throughout the setting up process there were certain uncertainties even if everything was working as expected or there were some errors.
- Another challenge tackled was implementation of the exponentially varying width in the model. This involved re-deriving the mode shape equations.
- Some of the computations were extremely costly. This occurred mainly in the optimization part of this thesis. While performing the optimization, multiple iterations needed to be performed and each iteration involved calculation of multiple terms which was very time consuming.
- It was possible to reduce the computation time of some of the expressions by converting them into explicit equations instead of integration equations. Mathematica was used to convert the integral equations into explicit equations.
- It was observed that both electrical and mechanical damping play a crucial part in the model validation process. Having an optimal value of both would help obtain a better model validation.

- From the optimization section it was observed that the voltage increases with the length of the beam (L_B) and delta (δ), while the length of the patch doesn't play much role in the optimum value of voltage.
- In order to reduce the computation time of certain calculations ERAU Vega super computer was used.
- Having a varying cross section would increase the amount of energy harvested and hence could lead to a better design for the energy harvester.
- Though only a maximum of three constraints were added to the optimization problem it is possible to add more constraint to make the optimization problem even more rigorous.

5.3. Recommendations and Future Works

There were some limitations in the presented work due to time constraints, certain instrumentation problems and also because of limited knowledge on certain aspects of this research. Therefore, following are some of the recommendations for future work of this research:

- Though the mathematical model used was sufficient to perform the optimization it still was erroneous especially on frequencies below the natural frequency. An effort needs to be made so that the voltage can be exactly the same for both the experiment and the model.
- Better methods for obtaining the damping ratio.
- The peak voltage for model and experiment occurred at different frequencies the reason for this needs to be studied and hence corrected.

- Developing an FE model in any finite element software could also serve as another validation for the mathematical model or experiment results.
- The optimization was more open-ended and therefore having a closer ended optimization would be beneficial.
- In this thesis on a maximum of three design variables were used for the optimization problem. The implementation of more design variables could be an excellent extension of this work.
- The thickness was kept constant throughout this thesis, studying the effect of thickness of voltage could also be another aspect to look into.
- Lastly, validation of the optimization results against an experiment would be extremely necessary.

REFERENCES

- Abdelkefi, A., Najar, F., Nayfeh, A. H., & Ayed, S. B. (2011). An energy harvester using piezoelectric cantilever beams undergoing coupled bending–torsion vibrations. *Smart Materials and Structures*, 20(11), 115007.
- Ali, W. G., & Ibrahim, S. W. (2012). Power Analysis for piezoelectric energy harvester.
- Anton, S. R., & Sodano, H. A. (2007). A review of power harvesting using piezoelectric materials (2003-2006). *Smart materials and Structures*, 16(3), R1.
- Aridogan, U., Basdogan, I., & Erturk, A. (2014). Analytical modelling and experimental validation of a structurally integrated piezoelectric energy harvester on a thin plate. *Smart Materials and Structures*, 23(4), 045039.
- Beeby, S.P., Tudor, M. J., & White, N. M. (2006). Energy harvesting vibration sources for microsystems applications. *Measurement science and technology*, 17(12), R175.
- Cranch, E. T., & Adler, A. A. (1956). Bending vibrations of variable section beams. *Journal of Applied Mechanics*, 23(1), 103-108.
- Crawley, E. F., & Anderson, E. H. (1990). Detailed models of piezoceramic actuation of beams. *Journal of Intelligent Material Systems and Structures*, 1(1), 4-25.
- Curie, J., & Curie, P. (1880). Développement par compression de l'électricité polaire dans les cristaux hémihédres à faces inclinées. *Bulletin de minéralogie*, 3(4), 90-93.
- Dietl, J. M., & Garcia, E. (2010). Beam shape optimization for power harvesting. *Journal of Intelligent Material Systems and Structures*, 21(6), 633-646.
- Dow, A. B. A., Schmid, U., & Kherani, N. P. (2014). Unimorph and bimorph piezoelectric energy harvesters stimulated by β - emitting radioisotopes: a modeling study. *Microsystem technologies*, 20(4-5), 933-944.
- Ece, M. C., Aydogdu, M., & Taskin, V. (2007). Vibration of a variable cross-section beam. *Mechanics Research Communications*, 34(1), 78-84.
- Erturk, A., & Inman, D. J. (2008). A distributed parameter electromechanical model for cantilevered piezoelectric energy harvesters. *Journal of vibration and acoustics*, 130(4).
- Friswell, M. I., & Adhikari, S. (2010). Sensor shape design for piezoelectric cantilever beams to harvest vibration energy. *Journal of Applied Physics*, 108(1), 014901.
- Frontoni, E., Mancini, A., Zingaretti, P., & Gatto, A. (2013). Energy harvesting for smart shoes: A real life application. *ASME 2013 International Design Engineering*

- Technical Conferences and Computers and Information in Engineering Conference*. American Society of Mechanical Engineers Digital Collection.
- Gonzalez, C. G., Shiki, S. B., Brennan, M. J., da Silva, S., & Juni, V. L. (2010, September). Piezoelectric energy harvesting system optimization. In *2nd international conference on engineering optimization*. Lisbon, Portugal (pp. 1-8).
- Hagood, N. W., Chung, W. H., & Von Flotow, A. (1990). Modelling of piezoelectric actuator dynamics for active structural control. *Journal of intelligent material systems and structures*, 1(3), 327-354.
- High, J. W. (2003). *Method of fabricating NASA-standard macro-fiber composite piezoelectric actuators*. National Aeronautics and Space Administration, Langley Research Center.
- Hook, J. R., & Hall, H. E. (2010). *Solid State Physics 2nd edition*. Manchester, UK: Manchester Physics Series.
- Junior, C. D. M., Erturk, A., & Inman, D. J. (2009). An electromechanical finite element model for piezoelectric energy harvester plates. *Journal of Sound and Vibration*, 327(1-2), 9-25.
- Kovalovs, A., Barkanov, E., & Gluhihs, S. (2007). Active control of structures using micro-fiber composites (MFC). In *Journal of Physics: Conference Series* (Vol. 93, No. 1, p. 012034). IOP Publishing
- Kubba, A. E., & Jiang, K. (2014). A comprehensive study on technologies of tyre monitoring systems and possible energy solutions. *Sensors*, 14(6), 10306-10345.
- Liao, Y., & Sodano, H. A. (2008). Model of a single mode energy harvester and properties for optimal power generation. *Smart Materials and Structures*, 17(6), 065026.
- Meier, R., Kelly, N., Almog, O., & Chiang, P. (2014, August). A piezoelectric energy-harvesting shoe system for podiatric sensing. In *2014 36th Annual International Conference of the IEEE Engineering in Medicine and Biology Society* (pp. 622 – 625). IEEE.
- Ohanian, O., Hickling, C., Stiltner, B., Karni, E., Kochersberger, K., Probst, T., & Blain, A. (2012, April). Piezoelectric morphing versus servo-actuated MAV control surfaces. In *53rd AIAA/ASME/ASCE/AHS/ASC Structures, Structural Dynamics and Materials Conference 20th AIAA/ASME/AHS Adaptive Structures Conference 14th AIAA* (p. 1512).
- Ottman, G. K., Hofmann, H. F., & Lesieutre, G. A. (2002, June). Optimized piezoelectric energy harvesting circuit using step-down converter in discontinuous conduction

- mode. In *2002 IEEE 33rd Annual IEEE Power Electronics Specialists Conference. Proceedings (Cat. No. 02CH37289)* (Vol. 4, pp. 1988-1994). IEEE.
- Saadon, S., & Sidek, O. (2011). A review of vibration-based MEMS piezoelectric energy harvesters. *Energy conversion and management*, 52(1), 500-504.
- Shenck, N. S., & Paradiso, J.A. (2001). Energy Scavenging with Shoe-Mounted Piezoelectrics. *IEEE Micro*, 21(3), 30-42.
- Shen, D., Ch.oe, S. Y., & Kim, D.J. (2007). Analysis of piezoelectric materials for energy harvesting devices under high-g applications. *Japanese Journal of Applied Physics*, 46(10R), 6755.
- Sodano, H. A, Inman, D. J., & Park, G. (2004). A review of power harvesting from vibration using piezoelectric materials. *Shock and Vibration Digest*, 36(3), 197-206.
- Song, H. J., Choi, Y. T., Wereley, N. M., & Purekar, A. S. (2007, January). Analysis of energy harvesting devices using macro-fiber composite materials. In *ASME 2007 International Design Engineering Technical Conferences and Computers and Information in Engineering Conference* (pp. 289-298). American Society of Mechanical Engineers Digital Collection.
- Tabatabaei, S. M. K., Behbahani, S., & Rajaeipour, P. (2016). Multi-objective shape design optimization of piezoelectric energy harvester using artificial immune system. *Microsystem Technologies*, 22(10), 2435-2446.
- Tichý, J., Erhart, J., Kittinger, E., & Přívratská, J. (2010). *Fundamentals of piezoelectric sensorics: mechanical, dielectric, and thermodynamical properties of piezoelectric materials*. Springer Science & Business Media.
- Tong, X., Tabarrok, B., & Yeh, K. Y. (1995). Vibration analysis of Timoshenko beams with non-homogeneity and varying cross-section. *Journal of sound and vibration*, 186(5), 821-835.
- Umeda, M., Nakamura, K., & Ueha, S. (1996). Analysis of the transformation of mechanical impact energy to electric energy using piezoelectric vibrator. *Japanese Journal of Applied Physics*, 35(5S), 3267.
- Xu, B., & Li, Y. (2019). Force Analysis and Energy Harvesting for Innovative Multi-functional Shoes. *Frontiers in Materials*, 6, 221.
- Yang, Y., Tang, L., & Li, H. (2009). Vibration energy harvesting using macro-fiber composites. *Smart materials and structures*, 18(11), 115025.

Appendix A: FMINCON Options

The following table gives a list of options available with FMINCON (note: all default options were used)

Options	Defaults	Alternatives
Algorithm	Interior-point	Trust-region-reflective SQP SQP-legacy Active-set
CheckGradients	0 (false)	1 (True)
ConstraintTolerance	1.0000e-06	Open ended (smaller the better)
Display	Final	off or none iter iter-detailed notify notify-detailed final final-detailed
FiniteDifferenceStepSize	Sqrt(eps)	Can be scalar or vector (smaller the better)
FiniteDifferenceType	Forward	Central
HessianApproximation	bfgs	(only for interior –point) Finite-difference lbfgs
HessianFcn	[]	-
HessianMultiplyFcn	[]	-
HonorBounds	1	-
MaxFunctionEvaluations	3000	3000 (interior-point) 100*no.of variables (all other algorithms)
MaxIterations	1000	1000(interior-point) 400 (all other algorithms)
ObjectiveLimit	-1.0000e+20	Must be a scalar (only applicable to interior-point)
OptimalityTolerance	1.0000e-06	Must be a scalar (smaller the better)
OutputFcn	[]	-
PlotFcn	[]	Optimplotx Optimplotfunccount

		Optimplotfval Optimplotfvalconstr Optimplotconstrviolation Optimplotstepsize optimplotfirstorder
ScaleProblem	0 (False)	1 (true)
SpecifyConstraintGradient	0	1 (true)
SpecifyObjectiveGradient	0	1 (true)
StepTolerance	1.0000e-10	1e-10 (interior-point) 1e-6 (all other algorithms)
SubproblemAlgorithm	Factorization	(Only applicable to interior point) 'cg'
TypicalX	Ones(numberofvariables,1)	-
UseParallel	0 (False)	1 (true)